INTERNATIONAL JOURNAL FOR NUMERICAL METHODS IN ENGINEERING
Int. J. Numer. Meth. Engng 2006; **65**:1028–1067
Published online 19 September 2005 in Wiley InterScience (www.interscience.wiley.com). DOI: 10.1002/nme.1472

Extended Voronoi cell finite element model for multiple cohesive crack propagation in brittle materials

Shanhu Li and Somnath Ghosh*, †

Department of Mechanical Engineering, The Ohio State University, 650 Ackerman Road, Columbus, OH 43202, U.S.A.

SUMMARY

This paper introduces an extended Voronoi cell finite-element model (X-VCFEM) for modelling cohesive crack propagation in brittle materials with multiple cracks. The cracks are modelled by a cohesive zone model and their incremental directions and growth lengths are determined in terms of the cohesive energy near the crack tip. Extension to VCFEM is achieved through enhancements in stress functions in the assumed stress hybrid formulation. In addition to polynomial terms, the stress functions include branch functions in conjunction with level set methods, and multi-resolution wavelet functions in the vicinity of crack tips. The wavelet basis functions are adaptively enriched to accurately capture crack-tip stress concentrations. Conditions and methods of stability are enforced in X-VCFEM for improved convergence with propagating cracks. Two classes of problems are solved and compared with existing solutions in the literature for validation of the X-VCFEM algorithms. The first set corresponds to results for static cracks, while in the latter set, the propagation of cohesive cracks are considered. Comparison of X-VCFEM simulation results with results in literature for several fracture mechanics problems validates the effectiveness of X-VCFEM. Copyright © 2005 John Wiley & Sons, Ltd.

KEY WORDS: Voronoi cell finite-element model; multi-resolution wavelets; level set methods; cohesive zone model

1. INTRODUCTION

The past a few decades have witnessed increasing emphasis on the analysis of crack initiation and propagation in materials for effective design of high performance and reliable structural components. The difficulty in obtaining analytical solutions for many of these problems,

*Correspondence to: Somnath Ghosh, Department of Mechanical Engineering, The Ohio State University, 650, Ackerman Road, Columbus, OH 43202, U.S.A.
†E-mail: ghosh.5@osu.edu

Contract/grant sponsor: Air Force Office of Scientific Research; contract/grant number: F49620-98-1-01-93
Contract/grant sponsor: Army Research Office; contract/grant number: DAAD19-02-1-0428
Contract/grant sponsor: Ohio Supercomputer Center; contract/grant number: PAS813-2

Received 22 July 2005
Accepted 22 July 2005

Copyright © 2005 John Wiley & Sons, Ltd.

especially those associated with crack propagation, has prompted the use of numerical methods like the finite-element method (FEM) for the determination of fracture mechanics parameters such as stress intensity factors, energy release rates and *J*-integrals, crack-tip stresses and opening displacements. Analyses using conventional FEM require very high density mesh to overcome limitations of severe pathological mesh dependence near the crack tips. Convergence is very slow since stress singularities are not accounted for in the element formulation. For improving the computational efficiency through better representation of the crack-tip singularity, a number of different methods have been proposed. The superposition method [1, 2] has introduced the superposition of singular terms to the finite-element interpolations. The singular element method introducing the quarter-point elements [3–6] near the crack tip has been developed to yield reasonably accurate crack-tip parameters and displacements. As an alternative to the displacement-based FEMs, hybrid singular elements have been proposed in References [7–12]. Also termed as super-elements, these elements accommodate crack-tip singularity through interpolation functions that account for stress intensity factors using classical elasticity theory. Most of these analyses have been limited to stationary cracks and efficient methods for the analysis of propagating cracks have been limited until recently.

With increasing power of computational modelling and hardware, the cohesive zone models [13–20] have emerged as important tools for modelling crack propagation in homogeneous and heterogeneous materials. In these models, interfaces of similar and dissimilar materials are treated as zero thickness non-linear springs. Interfacial traction is specified as non-linear functions of tangential and normal separations across the interface to manifest crack evolution. These models have been used to simulate crack growth between elements in References [19, 21, 22], by lacing the interface between contiguous elements with cohesive springs. However, very often these models require highly refined computational mesh to control the direction of crack propagation. To avert this, intra-element enrichment approaches have been proposed, and a cogent review of some of these methods is provided in Reference [23]. Significant advances have been made in the modelling of propagation of strong and weak discontinuities with the these approaches, based on the incorporation of embedded discontinuities in the displacement or strain fields of an element. This can eliminate the need for remeshing and consequently mesh dependence in the prediction of the evolving crack path. Recently this approach has been consolidated by Moës, Belytschko and co-workers to propose an enhanced tool in the form of an extended FEM or X-FEM for modelling cohesive crack propagation [24–27]. The use of the partition of unity concept for incorporating local enrichment functions in X-FEM formulation allows the preservation of the general displacement-based FEM formalism.

Stress-based FEMs have had considerable success when stress fields are of interest in the analysis [7, 8]. Within this general formalism, the Voronoi cell FEM (VCFEM) has been developed in References [28–34] for micromechanical analysis of arbitrary heterogeneous microstructures. The method can effectively overcome requirements of large degrees of freedom in conventional FE models. Morphological arbitrariness in dispersions, shapes and sizes of heterogeneities, as seen in real micrographs are readily modelled by this method. The VCFE model naturally evolves by tessellation of the microstructure into a network of multi-sided Voronoi polygons. Each Voronoi cell with embedded heterogeneities (particle, fibre, void, crack, etc.) represents the region of contiguity for the heterogeneity, and is treated as an element in VCFEM. VCFEM elements are considerably larger than conventional FEM elements and incorporate a special assumed stress hybrid FEM formulation. Incorporation of known functional forms from

Copyright © 2005 John Wiley & Sons, Ltd.

analytical micromechanics substantially enhances its convergence. A high level of accuracy with significantly reduced degrees of freedom has been achieved with VCFEM. Computational efficiency is therefore substantially enhanced compared to conventional displacement-based FE models. Successful applications of 2D-small deformation VCFEM have been made in thermo-elastic-plastic problems of composite and porous materials [29, 30]. An adaptive VCFEM has been developed in Reference [30], where optimal improvement is achieved by *h–p* adaptation of the displacement field and *p*-enrichment of the stress field. Mechanisms of microstructural damage inception and growth in the form of inclusion cracking and interfacial debonding have also been incorporated in this formulation in References [28, 31, 34].

The cohesive crack propagation model has been incorporated in VCFEM in References [28, 34] to model interfacial debonding in fibre-reinforced composites. However, in these models, the debonding or crack evolution path is along the interface and hence the cohesive zone regions are known *a priori*. In the event that the crack branches off into the matrix, the path is no longer pre-assessed and needs to be determined at each load increment, consistent with the local state of stresses, strains and morphology. This task is considerably more challenging since a slight deviation can lead to completely wrong prediction.

The motivation of the present paper is derived from the need to create a robust VCFE model for arbitrary crack propagation in a monolithic matrix. An extended VCFEM or X-VCFEM is proposed for modelling the evolution of multiple cohesive cracks. This is an essential step, prior to simulating the entire microstructural failure problem in heterogeneous materials. X-VCFEM incorporates: (a) stress discontinuities across the cohesive crack through branch functions in conjunction with level set methods, (b) crack-tip stress concentration through the introduction of multi-resolution wavelet functions [35–37] in the vicinity of the crack tip, and (c) incremental crack propagation using a cohesive energy-based criterion for estimating the direction and length of the incremental crack advance. The paper begins with the extended Voronoi cell formulation for materials with multiple growing cracks. Enrichment of stress fields using level set method-based branch functions and wavelet functions are discussed. The methods of algorithms implementation and solution are discussed next with a discussion on the stability conditions. A number of numerical example are solved to demonstrate the effectiveness of this model.

2. VCFEM FORMULATION FOR MULTIPLE PROPAGATING CRACKS

The VCFE mesh for a brittle matrix with a dispersion of pre-existing cracks is shown in Figure 1(a). The typical Voronoi cell mesh corresponds to an unstructured mesh that is generated by Dirichlet or Voronoi tessellation of the domain, based on the position, shape and size of heterogeneities (inclusion, void, crack, etc.). Various tessellation schemes have been discussed and developed in References [28, 29]. While the name Voronoi cell has been historically used because of its association with point seeds in the generation process, the cells used in VCFEM may be variants of this construct. Essentially they represent neighbourhood or regions of influence for each heterogeneity. Subsequently the VCFE formulation considers each cell as a super-element consisting of a heterogeneity and its neighbourhood surrounding matrix [29, 30] without any further subdivision. The interfacial debonding analyses in References [28, 34] invoke the cohesive zone models to represent the growth of interfacial crack. However the main difference between that formulation and the present one is that, in the present case the

Copyright © 2005 John Wiley & Sons, Ltd.

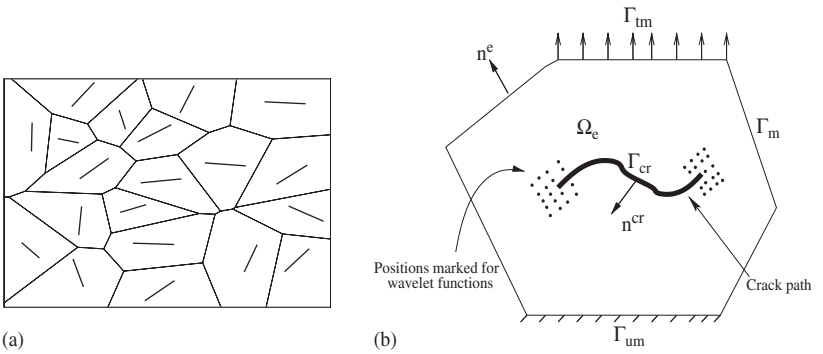

Figure 1. (a) A mesh of Voronoi cell elements, each containing a single pre-existing crack; and (b) a typical Voronoi cell element showing different topological features and loads.

path of the crack is arbitrary and is *a priori* unknown. This poses significant challenges that have been overcome with the X-VCFEM formulation.

Consider a pre-cracked microstructural region Ω consisting of N cracks as shown in Figure 1(a). The region is divided into an unstructured finite element mesh of arbitrary Voronoi cells. A typical VC element Ω_e containing a crack and its neighbouring matrix is depicted in Figure 1(b). The element boundary $\partial\Omega_e$ with outward normal $\mathbf{n}^E$ may consist of regions of prescribed traction Γ_{te}, prescribed displacement Γ_{ue} and inter-element edges Γ_{me}, i.e. $\partial\Omega_e^E = \Gamma_{te} \cup \Gamma_{ue} \cup \Gamma_{me}$. Furthermore, each element consists of a crack containing a fracture process zone that is represented by a cohesive zone model. The incompatible displacement field across the crack Γ_{cr} is facilitated through a set of connected node-pairs along the crack length. The node-pair merges at the crack tip by enforcing the same displacement. The normal along the crack path is denoted by $\mathbf{n}^{\mathrm{cr}}$. For the VCFEM element formulation, the micromechanics boundary value problem is described as

$$\text{Find}(\boldsymbol{\sigma}, \mathbf{u}^E, \mathbf{u}^{\mathrm{cr}}) \in \mathscr{T} \times \mathscr{V}^E \times \mathscr{V}^{\mathrm{cr}} \text{ satisfying}$$

$$\nabla \cdot \boldsymbol{\sigma} + \bar{\mathbf{f}} = \mathbf{0} \quad \text{and} \quad \frac{\partial B}{\partial \boldsymbol{\sigma}} = \boldsymbol{\varepsilon} \in \Omega_e \tag{1a}$$

$$\mathbf{u}^E = \bar{\mathbf{u}} \quad \text{on } \Gamma_{ue}, \quad \boldsymbol{\sigma} \cdot \mathbf{n}^E = \bar{\mathbf{t}} \quad \text{on } \Gamma_{te} \quad \text{and} \quad \boldsymbol{\sigma} \cdot \mathbf{n}^{\mathrm{cr}} = \mathbf{t}^{\mathrm{coh}} \quad \text{on } \Gamma_{\mathrm{cr}} \tag{1b}$$

The variables $\boldsymbol{\sigma}$, $\boldsymbol{\varepsilon}$, B and $\mathbf{f}$ are the equilibrated stress fields, the corresponding strain fields, the complimentary energy and body forces per unit volume, respectively, in the element interior. $\mathscr{T}$, $\mathscr{V}^E$ and $\mathscr{V}^{\mathrm{cr}}$ correspond to Hilbert spaces containing the stress and displacement solutions, respectively. $\mathbf{u}^E$ is the kinematically admissible displacement field on the element boundary $\partial\Omega_e^E$ and $\mathbf{u}^{\mathrm{cr}}$ represents the displacements on the internal cohesive-crack surfaces Γ_{cr}. Variables with superscript E are on the element boundary while those with superscripts cr correspond to the crack surface. The traction $\mathbf{t}^{\mathrm{coh}}$ between node-pairs on the crack surface are modelled by the cohesive zone traction-separation law. The VCFEM formulation is based on the assumed stress hybrid FEM, in which stationarity conditions of the element energy functional in the variational principle yields weak forms of the kinematic equation and traction reciprocity conditions, as Euler equations. In the small deformation elasticity incremental formulation for

Copyright © 2005 John Wiley & Sons, Ltd.

evolving cracks, the element energy functional Π_e is defined in terms of increments of stresses and displacements as

$$\begin{aligned}
&\Pi_e(\sigma_{ij}, \Delta\sigma_{ij}, u_i^E, \Delta u_i^E, u_i^{\mathrm{cr}}, \Delta u_i^{\mathrm{cr}}) \\
&= -\int_{\Omega_e} \Delta B(\sigma_{ij}, \Delta\sigma_{ij})\,\mathrm{d}\Omega - \int_{\Omega_e} \varepsilon_{ij}\Delta\sigma_{ij}\,\mathrm{d}\Omega \\
&\quad + \int_{\partial\Omega_e} (\sigma_{ij} + \Delta\sigma_{ij}) n_j^E (u_i^E + \Delta u_i^E)\,\mathrm{d}\partial\Omega - \int_{\Gamma_{tm}} (\bar{t}_i + \Delta\bar{t}_i)(u_i^E + \Delta u_i^E)\,\mathrm{d}\Gamma_{te} \\
&\quad + \int_{\Gamma_{\mathrm{cr}}^1} (\sigma_{ij} + \Delta\sigma_{ij}) n_j^{\mathrm{cr}} (\overset{1}{u}{}_i^{\mathrm{cr}} + \Delta\overset{1}{u}{}_i^{\mathrm{cr}})\,\mathrm{d}\Gamma_{\mathrm{cr}} - \int_{\overset{2}{\Gamma}_{\mathrm{cr}}} (\sigma_{ij} + \Delta\sigma_{ij}) n_j^{\mathrm{cr}} (\overset{2}{u}{}_i^{\mathrm{cr}} + \Delta\overset{2}{u}{}_i^{\mathrm{cr}})\,\mathrm{d}\Gamma_{\mathrm{cr}} \\
&\quad - \int_{\Gamma_{\mathrm{cr}}} \int_{\overset{1}{u}{}_i^{\mathrm{cr}} - \overset{2}{u}{}_i^{\mathrm{cr}}}^{\overset{1}{u}{}_i^{\mathrm{cr}} + \Delta\overset{1}{u}{}_i^{\mathrm{cr}} - \overset{2}{u}{}_i^{\mathrm{cr}} - \Delta\overset{2}{u}{}_i^{\mathrm{cr}}} t_i^{\mathrm{coh}} d(\overset{1}{u}{}_i^{\mathrm{cr}} - \overset{2}{u}{}_i^{\mathrm{cr}})\,\mathrm{d}\Gamma_{\mathrm{cr}}
\end{aligned} \tag{2}$$

where $B = \frac{1}{2}\boldsymbol{\sigma} : \mathbf{S} : \boldsymbol{\sigma}$ is the complimentary energy density and $\Delta B(\sigma_{ij}, \Delta\sigma_{ij})$ is its increment due to stress increase. $\mathbf{S}$ is the material compliance matrix. The notations $\overset{1}{(\bullet)}$ and $\overset{2}{(\bullet)}$ represent two sides of the internal cohesive crack surface. The last term provides the work done by the cohesive tractions t_i^{coh} due to crack surface separation. In VCFE formulation, the equilibrium conditions and constitutive relations in the matrix and the compatibility conditions on the element boundary and crack surface are satisfied *a priori* in a strong sense. The element kinematic equation:

$$\nabla \mathbf{u}_e = \boldsymbol{\varepsilon}_e \quad \text{in } \Omega_e \tag{3}$$

is however satisfied in a weak sense from the stationary condition of the element energy functional in Equation (2). The weak form is obtained by setting the first variation of Π_e with respect to stress increments to zero, i.e.

$$\begin{aligned}
&-\int_{\Omega_e} \left(\frac{\partial \Delta B}{\partial \Delta\sigma_{ij}} + \varepsilon_{ij} \right) \delta\Delta\sigma_{ij}\,\mathrm{d}\Omega + \int_{\partial\Omega_e} \delta\Delta\sigma_{ij} n_j^e (u_i^E + \Delta u_i^E)\,\mathrm{d}\partial\Omega_e \\
&\quad + \int_{\overset{1}{\Gamma}_{\mathrm{cr}}} \delta\Delta\sigma_{ij} n_j^{\mathrm{cr}} (\overset{1}{u}{}_i^{\mathrm{cr}} + \Delta\overset{1}{u}{}_i^{\mathrm{cr}})\,\mathrm{d}\Gamma_{\mathrm{cr}} - \int_{\overset{2}{\Gamma}_{\mathrm{cr}}} \delta\Delta\sigma_{ij} n_j^{\mathrm{cr}} (\overset{2}{u}{}_i^{\mathrm{cr}} + \Delta\overset{2}{u}{}_i^{\mathrm{cr}})\,\mathrm{d}\Gamma_{\mathrm{cr}} = 0
\end{aligned} \tag{4}$$

Solution of Equation (4) yields domain stresses. Furthermore, the VCFE formulation assumes weak satisfaction of the traction reciprocity conditions on (i) the inter-element boundary Γ_{me}, and (ii) the domain traction boundary Γ_{te} and (iii) the crack surfaces $\overset{1}{\Gamma}_{\mathrm{cr}}$ and $\overset{2}{\Gamma}_{\mathrm{cr}}$:

$$(\sigma_{ij} + \Delta\sigma_{ij}) n_j^{E+} = -(\sigma_{ij} + \Delta\sigma_{ij}) n_j^{E-} \quad \text{on } \Gamma_{me} \text{ (inter-element boundary)}$$

Copyright © 2005 John Wiley & Sons, Ltd.

$$(\sigma_{ij} + \Delta\sigma_{ij})n_j^E = \bar{t}_i + \Delta\bar{t}_i \quad \text{on } \Gamma_{te} \text{ (traction boundary)} \tag{5}$$

$$(\sigma_{ij} + \Delta\sigma_{ij})^1 n_j^{\text{cr}} = (\sigma_{ij} + \Delta\sigma_{ij})^2 n_j^{\text{cr}} \quad \text{on } \Gamma_{\text{cr}}$$

In the variational principle, the weak form is obtained by setting the first variation of the total energy functional $\Pi = \sum_{e=1}^{N} \Pi_e$ with respect to the displacements $\Delta\mathbf{u}^E$, $\Delta\overset{1}{\mathbf{u}}^{\text{cr}}$ and $\Delta\overset{2}{\mathbf{u}}^{\text{cr}}$, respectively, to zero, or

$$\sum_{e=1}^{N} \int_{\partial\Omega_e} [(\sigma_{ij} + \Delta\sigma_{ij})n_j^e \delta u_i^E \, \mathrm{d}\partial\Omega - \int_{\Gamma_{tm}} (\bar{t}_i + \Delta\bar{t}_i)]\delta u_i^E \, \mathrm{d}\Gamma_{tm} = 0$$

$$\forall \delta\mathbf{u}_e^E \in \bar{\mathscr{V}}_e^E = \{\mathbf{v}_e^E \in \mathscr{H}^o(\partial\Omega_e^E) : \mathbf{v}_e^E = \mathbf{0} \text{ on } \Gamma_{ue}\} \quad \forall e \text{ on } \partial\Omega_e \tag{6}$$

$$\int_{\overset{1}{\Gamma}_{\text{cr}}} [(\sigma_{ij} + \Delta\sigma_{ij})n_j^{\text{cr}} - \phi_i']\delta\overset{1}{u}_i^{\text{cr}} \, \mathrm{d}\Gamma_{\text{cr}} = 0 \quad \text{and} \quad \int_{\overset{2}{\Gamma}_{\text{cr}}} [(\sigma_{ij} + \Delta\sigma_{ij})n_j^{\text{cr}} + \phi_i']\delta\overset{2}{u}_i^{\text{cr}} \, \mathrm{d}\Gamma_{\text{cr}} = 0$$

$$\forall \delta\mathbf{u}_e^{\text{cr}} \in \mathscr{V}_e^{\text{cr}} \quad \forall e \text{ on } \Gamma_{\text{cr}} \tag{7}$$

where $\phi = \int_{\overset{1}{u}_i^{\text{cr}} - \overset{2}{u}_i^{\text{cr}}}^{\overset{1}{u}_i^{\text{cr}} + \Delta\overset{1}{u}_i^{\text{cr}} - \overset{2}{u}_i^{\text{cr}} - \Delta\overset{2}{u}_i^{\text{cr}}} t_i^{\text{coh}} d(\overset{1}{u}_i^{\text{cr}} - \overset{2}{u}_i^{\text{cr}})$ is the cohesive energy function and $\phi_i' = \partial\phi/\partial u_i^{\text{cr}}$.

2.1. Cohesive zone models for crack propagation

Cohesive zone models, introduced in References [38, 39] and developed in References [13–20], are effective in depicting material failure as a separation process across an extended crack tip or fracture process zone. In these models, the tractions across the crack reach a maximum, subsequently decrease and eventually vanish with increasing separation across the crack. The cohesive model used in this paper is a three parameter rate independent linear cohesive model, proposed in References [19, 20]. This is an extrinsic (two stage) model which has an infinite stiffness or slope in the rising portion of the traction-separation law upto a peak traction value. This is followed by linear descending segment till a zero traction value is reached. The model assumes a free cohesive energy potential ϕ such that the traction across the cohesive surface is expressed as

$$\mathbf{t}^{\text{coh}} = \frac{\partial\phi}{\partial\delta_n}\mathbf{n} + \frac{\partial\phi}{\partial\delta_t}\mathbf{t} \tag{8}$$

Here δ_n and δ_t correspond to the normal and tangential components of the opening displacements over the cohesive surface in the $\mathbf{n}$ and $\mathbf{t}$ directions, respectively. An effective opening displacement is defined as

$$\delta = \sqrt{\delta_n^2 + \beta^2\delta_t^2} \tag{9}$$

Copyright © 2005 John Wiley & Sons, Ltd.

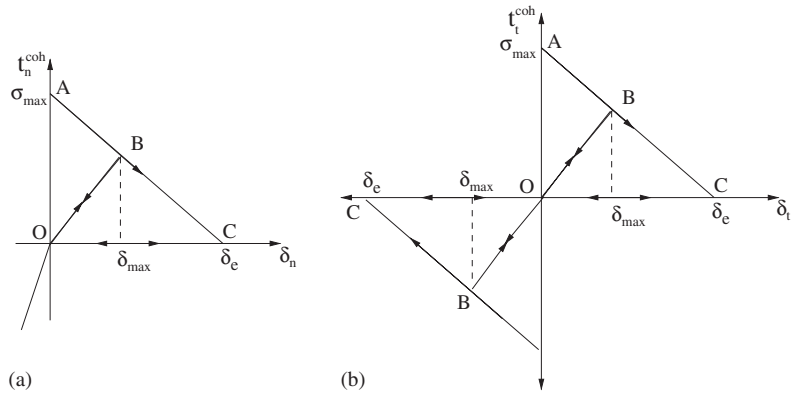

Figure 2. Normal and tangential traction-separation behaviour for the linear cohesive zone model.

where β is a coupling coefficient to allow assignment of different weights to normal and tangential opening displacements. Consequently the cohesive surface traction reduces to

$$\mathbf{t}^{\text{coh}} = \frac{t}{\delta}(\beta^2 \delta_t \mathbf{t} + \delta_n \mathbf{n}) \quad \text{where } t = \frac{\partial \phi}{\partial \delta} = \sqrt{t_n^{\text{coh}2} + \beta^{-2} t_t^{\text{coh}2}} \tag{10}$$

where t_n^{coh} and t_t^{coh} are the normal and tangential components of surface tractions. The effective cohesive force t in this model for increasing δ takes the form

$$t = \begin{cases} \dfrac{\sigma_{\max}(\delta_e - \delta)}{\delta_e} & \forall \delta < \delta_e \\ 0 & \forall \delta \geqslant \delta_e \end{cases} \tag{11}$$

δ_e corresponds to the separation at which t goes to zero and $\sigma_{\max}$ is the peak value of t. The effective normal traction-separation response of this model is depicted in Figure 2. In the softening region, unloading from any point on the traction-separation curve, proceeds along a linear path from the current position to the origin as shown by the line BO in Figure 2. The corresponding t–δ relation is

$$t = \frac{\sigma_{\max}}{\delta_e} \frac{\delta_e - \delta_{\max}}{\delta_{\max}} \delta \quad \forall \delta \leqslant \delta_{\max} \leqslant \delta_e \tag{12}$$

Reloading follows the path OBC with a reduced stiffness in comparison with the original stiffness. Traction vanishes for $\delta \geqslant \delta_e$. For negative normal displacement (compression), stiff penalty springs with high stiffness are introduced between the node-pairs on the crack face. To define the tangent stiffness matrix, it is necessary to distinguish between crack initiation ($\delta = 0$) and crack propagation from an initialized state ($\delta > 0$). In the former, $t_n^{\text{coh}} = t$, and $t_t^{\text{coh}} = 0$ are assumed, which implies that the initiation is in pure mode I. The cohesive parameters in this study are calibrated from experiments done for epoxy–steel composites as discussed in References [28, 34].

Recent experimental–computational studies on composites, conducted in Reference [40] show that the three or four parameter cohesive models are more suitable for modelling interfacial

Copyright © 2005 John Wiley & Sons, Ltd.

debonding in comparison with the two parameter models based on Ferrante's law [13–15]. Similar conclusions have also been drawn in the work by Ghosh *et al*. [28] and Li and Ghosh [34], where bilinear cohesive models were chosen to study interfacial debonding in fibre-reinforced composites.

2.2. General element assumptions and weak form

In the absence of body forces, two-dimensional stress fields satisfying equilibrium relations can be generated from the Airy's stress function $\Phi(x, y)$. In the incremental formulation, stress increments are obtained from derivatives of the stress functions $\Delta\Phi(x, y)$ as

$$\begin{pmatrix} \Delta\sigma_{xx} \\ \Delta\sigma_{yy} \\ \Delta\sigma_{xy} \end{pmatrix} = \begin{pmatrix} \dfrac{\partial^2 \Delta\Phi}{\partial y^2} \\ \dfrac{\partial^2 \Delta\Phi}{\partial x^2} \\ -\dfrac{\partial^2 \Delta\Phi}{\partial x \partial y} \end{pmatrix} = [\mathbf{P}(x, y)]\{\Delta\beta\} \tag{13}$$

where $\{\Delta\beta\}$ is the column of unknown stress increment coefficients, associated with the stress interpolation matrix $[\mathbf{P}(x, y)]$. Convergence properties and efficiency of VCFEM depend on the choice of Φ. These functions should adequately account for the geometry and location of the heterogeneity in the element. Polynomial functions alone do not contribute to this requirement and hence lead to poor convergence [29, 30]. Consequently, stress functions in X-VCFEM are constructed from different expansion functions that have complementary effects on the solution convergence for the propagating crack. Compatible displacement fields satisfying inter-element continuity on the element boundary $\partial\Omega_e^E$ and intra-element continuity on the crack face Γ_{cr} are generated by interpolation of nodal displacements [28–30] as

$$\begin{aligned} \{\Delta u^e\} &= [\mathbf{L}_e]\{\Delta q^e\} \quad \text{on } \partial\Omega_e \\ \{\Delta \overset{1}{u}{}^{\text{cr}}\} &= [\overset{1}{\mathbf{L}}_{\text{cr}}]\{\Delta \overset{1}{q}{}^{\text{cr}}\} \quad \text{on } \overset{1}{\Gamma}_{\text{cr}} \\ \{\Delta \overset{2}{u}{}^{\text{cr}}\} &= [\overset{2}{\mathbf{L}}_{\text{cr}}]\{\Delta \overset{2}{q}{}^{\text{cr}}\} \quad \text{on } \overset{2}{\Gamma}_{\text{cr}} \end{aligned} \tag{14}$$

The interpolation matrices $[\mathbf{L}_e]$, $[\overset{1}{\mathbf{L}}_{\text{cr}}]$, $[\overset{2}{\mathbf{L}}_{\text{cr}}]$ for the nodal displacements on the respective boundaries are constructed using standard linear or hierarchical shape functions.

Remark

It is desirable that the displacement interpolations on the crack surface in Equation (14) have adequate resolution, consistent with the high resolution in the stress fields near the crack tip. To accommodate this, hierarchical shape functions are added to standard linear shape functions to describe displacements on the crack surface as

$$\mathbf{u}^{\text{cr}} = \sum_{i=1}^{4} N_i(s) * \mathbf{q}_i^{\text{cr}} \tag{15}$$

Copyright © 2005 John Wiley & Sons, Ltd.

where $N_1 = \frac{1}{2}(1-s)$, $N_2 = \frac{1}{2}(1+s)$, $N_3 = \frac{1}{2}(s^2-1)$, and $N_4 = \frac{1}{6}(s^3-s)$. The first two are the standard linear shape functions, while the last two are the hierarchical shape functions in natural coordinates s. The degrees of freedom corresponding to higher order shape functions (i.e. to quadratic, cubic, etc.) cannot be interpreted as nodal values of displacement. Instead, they are values of some higher order derivatives of the solution at the midpoints (or linear combination of these derivatives).

Substituting the interpolations of stress and displacement fields from Equations (13) and (14) into Equation (2) results in the matrix form of the element complimentary energy

$$\begin{aligned}\Pi_e = &-\frac{1}{2}\{\boldsymbol{\beta}+\Delta\boldsymbol{\beta}\}^{\mathrm{T}}[\mathbf{H}]\{\boldsymbol{\beta}+\Delta\boldsymbol{\beta}\}+\{\boldsymbol{\beta}+\Delta\boldsymbol{\beta}\}^{\mathrm{T}}[\mathbf{G}]^e\{\mathbf{q}^e+\Delta\mathbf{q}^e\}\\ &+\{\boldsymbol{\beta}+\Delta\boldsymbol{\beta}\}^{\mathrm{T}}[\overset{1}{\mathbf{G}}{}^{\mathrm{cr}}]\{\overset{1}{\mathbf{q}}{}^{\mathrm{cr}}+\Delta\overset{1}{\mathbf{q}}{}^{\mathrm{cr}}\}-\{\hat{\mathbf{t}}\}^{\mathrm{T}}\{\mathbf{q}^e+\Delta\mathbf{q}^e\}\\ &-\{\boldsymbol{\beta}+\Delta\boldsymbol{\beta}\}^{\mathrm{T}}[\overset{2}{\mathbf{G}}{}^{\mathrm{cr}}]\{\overset{2}{\mathbf{q}}{}^{\mathrm{cr}}+\Delta\overset{2}{\mathbf{q}}{}^{\mathrm{cr}}\}-\int_{\Gamma_{\mathrm{cr}}}\int_{\overset{1}{\mathbf{u}}{}^{\mathrm{cr}}-\overset{2}{\mathbf{u}}{}^{\mathrm{cr}}}^{\overset{1}{\mathbf{u}}{}^{\mathrm{cr}}+\Delta\overset{1}{\mathbf{u}}{}^{\mathrm{cr}}-\overset{2}{\mathbf{u}}{}^{\mathrm{cr}}-\Delta\overset{2}{\mathbf{u}}{}^{\mathrm{cr}}} t_i^{\mathrm{coh}}\,d(\overset{1}{u}{}_i^{\mathrm{cr}}-\overset{2}{u}{}_i^{\mathrm{cr}})\,\mathrm{d}\Gamma_{\mathrm{cr}} \end{aligned} \tag{16}$$

where

$$\begin{aligned}&[\mathbf{H}]=\int_{\Omega_e}[\mathbf{P}]^{\mathrm{T}}[\mathbf{S}][\mathbf{P}]\,\mathrm{d}\Omega \quad [\mathbf{G}^e]=\int_{\partial\Omega_e}[\mathbf{P}]^{\mathrm{T}}[\mathbf{n}^e][\mathbf{L}_e]\,\mathrm{d}\partial\Omega\\ &[\overset{1}{\mathbf{G}}{}^{\mathrm{cr}}]=\int_{\overset{1}{\Gamma}_{\mathrm{cr}}}[\mathbf{P}]^{\mathrm{T}}[\mathbf{n}^{\mathrm{cr}}][\overset{1}{\mathbf{L}}_{\mathrm{cr}}]\,\mathrm{d}\Gamma_{\mathrm{cr}} \quad [\overset{2}{\mathbf{G}}{}^{\mathrm{cr}}]=\int_{\overset{2}{\Gamma}_{\mathrm{cr}}}[\mathbf{P}]^{\mathrm{T}}[\mathbf{n}^{\mathrm{cr}}][\overset{2}{\mathbf{L}}_{\mathrm{cr}}]\,\mathrm{d}\Gamma_{\mathrm{cr}}\\ &\{\hat{\mathbf{t}}\}=\int_{\Gamma_{tm}}\{\bar{\mathbf{t}}+\Delta\bar{\mathbf{t}}\}^{\mathrm{T}}[\mathbf{n}^e][\mathbf{L}_e]\,\mathrm{d}\Gamma_{tm}\end{aligned} \tag{17}$$

Construction of appropriate stress functions with optimally high resolution is necessary for accurately depicting high stress gradients near the crack tip.

2.3. Stability conditions

Following the stability conditions derived for displacement- and stress-based finite element approximations in References [41–43], the stability conditions of the stress–displacement field variational problem in X-VCFEM depend on the following conditions:

- The matrix [**H**] should be positive definite. From the definition of [**H**] in Equation (17), the necessary condition for it to be positive definite is that the compliance tensor [**S**] be positive definite, which is true for elastic problems.
- A second condition is that the finite-dimensional stress subspaces $\mathscr{T}$ be spanned uniquely by the basis functions [**P**]. This is satisfied by assuring linear independence of the columns of basis functions [**P**], which also guarantees the invertibility of [**H**].
- Additional stability conditions should be satisfied to guarantee non-zero stress parameters $\boldsymbol{\beta}$ for all non-rigid body displacement fields on the element boundary $\mathbf{u}_e^E$ or on the crack face $\mathbf{u}_e^{\mathrm{cr}}$. This is accomplished by careful choice of the dimensions of the stress and

Copyright © 2005 John Wiley & Sons, Ltd.

displacement subspaces, i.e. $n_\beta > n_q^E + n_q^{\mathrm{cr}} - 3$, where n_β is the number of β parameters, and n_q^E and n_q^{cr} are the number of displacement degrees of freedom on the element boundary and crack face, respectively.

3. CREATION OF ENRICHED STRESS FUNCTIONS IN X-VCFEM

VCFEM formulations for micromechanical analysis of heterogeneous materials have incorporated polynomial and reciprocal stress functions based on analytical micromechanics results in References [28–31]. In the present work, the heterogeneity is in the form of an evolving cohesive crack. Two conditions need to be considered in the choice of stress functions. The first is that it should adequately represent crack-tip high stress concentration as required by the cohesive zone models. Polynomial functions alone are unable to satisfy this requirement and hence suffers from poor convergence. The second condition is that the stress function should account for stress jump across the crack surface. The stress functions in X-VCFEM incorporate three different components, namely: (a) a purely polynomial function Φ^{poly} to yield the far field stress distributions away from the crack tip, (b) a branch function Φ^{branch} that is constructed from level set functions, and (c) a multi-resolution wavelet function Φ^{wvlt} to account for the moving crack-tip stress concentration. Thus, $\Phi = \Phi^{\mathrm{poly}} + \Phi^{\mathrm{branch}} + \Phi^{\mathrm{wvlt}}$.

3.1. Pure polynomial forms of stress function

The pure polynomial component of the stress function Φ^{poly} is written in terms of scaled local coordinates ($\hat{\xi} = (x - x_c)/L$, $\hat{\eta} = (y - y_c)/L$) with origin at the element centroid (x_c, y_c), as

$$\Phi^{\mathrm{poly}}(\xi, \eta) = \sum_{p=0,q=0}^{p_n,q_n} \xi^p \eta^q \beta_{pq} \tag{18}$$

The scaling parameter in the coordinate representation is $L = \sqrt{\max(x - x_c) \times \max(y - y_c)}$ $\forall (x, y) \in \partial\Omega_e$. The use of the scaled local coordinates $(\hat{\xi}, \hat{\eta})$, as opposed to global coordinates (x, y) in the construction of stress functions, prevents ill conditioning of the [**H**] matrix due to the high exponents of (x, y) in Φ^{poly}. As discussed in Reference [44], invariance of stresses with respect to coordinate transformations can be ensured by a complete polynomial representation of Φ^{poly}, while stability of the algorithm requires linear independence of the columns of stresses derived from Φ^{poly}.

3.2. Branch stress functions using level set methods

The branch function Φ^{branch} facilitates jumps in stresses across the crack surfaces. These functions should not affect the solutions in the continuous region beyond the crack. This construction requires a functional representation of the surface or line of discontinuity. Level set methods, introduced by Adalsteinsson and Sethian [45] and Sethian [46] for following the evolution of interfaces, is ideal for representing arbitrary contours. The method has been used by Belytschko *et al*. [47] for the construction of branch functions associated with the partition of unity in a displacement-based FEM formulation. The standard level set methods invoke continuous evolution of the entire surface of discontinuity. However for problems involving cracks, the only evolution occurs at the crack tip and the crack surface needs to be frozen

Copyright © 2005 John Wiley & Sons, Ltd.

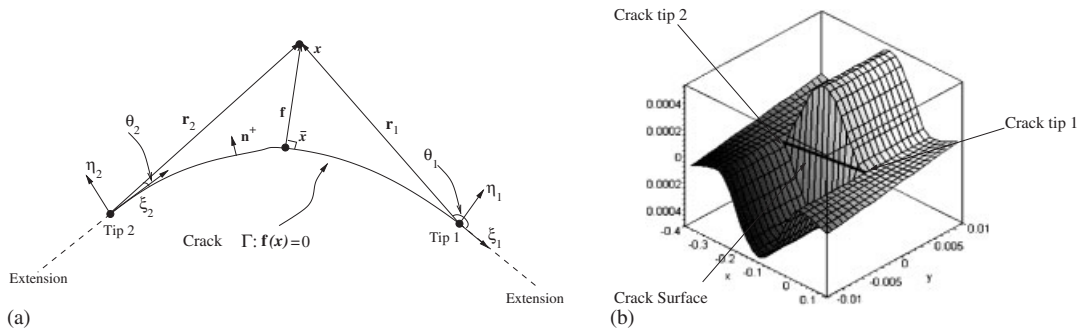

Figure 3. (a) A schematic diagram of a crack surface showing parameters related to the distance functions; and (b) depiction of the branched stress function Φ^{branch} near a crack for $s=0, t=0$.

behind tip. A vector level set method has been developed in References [48, 49] to freeze the crack surface in accordance with geometric updating. This method is used in this work.

An approximation to the crack surface Γ_{cr} in Figure 1 is constructed to describe the discontinuous stress fields across crack paths. As shown in Figure 3(a), the discontinuous surface is expressed by a signed distance function $f(\mathbf{x})$ defined as

$$f(\mathbf{x}) = \min_{\bar{\mathbf{x}} \in \Gamma} \|\mathbf{x} - \bar{\mathbf{x}}\| \text{sign}(\mathbf{n}^+ \cdot (\mathbf{x} - \bar{\mathbf{x}})) \tag{19}$$

where $\bar{\mathbf{x}}$ is a point on the surface of discontinuity and $\mathbf{n}^+$ is a unit normal pointing in the direction of the region of positive distance function. Consequently, $\bar{\mathbf{x}}$ is the closest point projection of any point $\mathbf{x}$ on Γ_{cr}. In order to describe the crack path accurately, the signed function $f(\mathbf{x})$ is evaluated at every integration point in the Voronoi cell element directly. The process of constructing branch functions involves steps that are described below.

- Radial distance functions to the two crack tips $r_1(\mathbf{x})$ and $r_2(\mathbf{x})$ and the corresponding angular positions $\theta_1(\mathbf{x})$ and $\theta_2(\mathbf{x})$ are depicted in Figure 3(a). These functions are expressed in terms of coordinates of local systems (ξ, η) with origins at the crack tips. For the local system at crack tip 1, the coordinates of $\mathbf{x}$ are (ξ_1, η_1). In accordance with the definition of the signed distance function, the radial distance and angle functions are expressed as

$$r_1(\mathbf{x}) = \sqrt{\xi_1^2 + \eta_1^2} \quad \text{and} \quad \theta_1(\mathbf{x}) = \begin{cases} \pi - \sin^{-1}\dfrac{f}{r_1}, & \xi_1 < 0, \quad f \geqslant 0 \\ -\sin^{-1}\dfrac{f}{r_1} - \pi, & \xi_1 < 0, \quad f < 0 \\ \sin^{-1}\dfrac{f}{r_1}, & \xi_1 \geqslant 0 \end{cases} \tag{20}$$

Copyright © 2005 John Wiley & Sons, Ltd.

Similarly, the radial distance and angle functions for the coordinate system at crack tip 2 are defined as

$$r_2(\mathbf{x}) = \sqrt{\xi_2^2 + \eta_2^2} \quad \text{and} \quad \theta_2(\mathbf{x}) = \begin{cases} \pi - \sin^{-1}\dfrac{f}{r_2}, & \xi_2 < 0, \quad f \geqslant 0 \\ -\sin^{-1}\dfrac{f}{r_2} - \pi, & \xi_2 < 0, \quad f < 0 \\ \sin^{-1}\dfrac{f}{r_2}, & \xi_2 \geqslant 0 \end{cases} \tag{21}$$

- The branched stress function is constructed in terms of the functions $f(\mathbf{x})$, θ_1, r_1, θ_2, and r_2, as

$$\Phi^{\text{branch}} = \sum_{s=0,t=0}^{s_n,t_n} r_1^2 \sin\frac{\theta_1}{2} r_2^2 \cos\frac{\theta_2}{2} \xi_1^s \eta_1^t \beta_{st} \tag{22}$$

The terms r_1^2 and r_2^2 in Φ^{branch} are necessary for avoiding crack-tip singularity in the stresses due to this function and for improving the accuracy. Along the tangential extension to the crack path at the tip 1, Φ^{branch} is zero since $\sin(\theta_1/2) = 0$. Hence Φ^{branch} does not contribute to the stresses ahead of the crack tip 1. In an analogous manner, Φ^{branch} goes to zero along the extension to the crack path at the tip 2, since $\cos(\theta_2/2) = 0$. Therefore Φ^{branch} does not contribute to the stresses in this region also. However, along the crack surface between the two crack tips, $\sin(\theta_1/2) = \pm 1$ on both sides of the crack, and $\cos(\theta_2/2) = 1$. This renders Φ^{branch} in Equation (22) discontinuous across the crack path. In Φ^{branch}, θ_1 is used to create the discontinuity across the crack surface, while θ_2 eliminates the discontinuity ahead of crack tip 2. In some special instances with only one crack tip such as a panel with an edge crack, Equation (22) may be simplified by removing r_2 and θ_2 dependence to yield

$$\Phi^{\text{branch}} = \sum_{s,t} r_1^2 \sin\frac{\theta_1}{2} \xi_1^s \eta_1^t \beta_{st} \tag{23}$$

A coordinate transformation is required to obtain stress components in the global coordinate system from $\Phi^{\text{branch}}(\xi, \eta)$ based on the local coordinate system.

$$\begin{bmatrix} \sigma_{xx} & \sigma_{xy} \\ \sigma_{xy} & \sigma_{yy} \end{bmatrix}^{\text{branch}} = [\mathbf{Q}_b]^{\mathrm{T}} \begin{bmatrix} \dfrac{\partial^2 \Phi^{\text{branch}}}{\partial \eta_1^2} & -\dfrac{\partial^2 \Phi^{\text{branch}}}{\partial \xi_1 \partial \eta_1} & & \\ -\dfrac{\partial^2 \Phi^{\text{branch}}}{\partial \xi_1 \partial \eta_1} & \dfrac{\partial^2 \Phi^{\text{branch}}}{\partial \xi_1^2} & & \\ & & \dfrac{\partial^2 \Phi^{\text{branch}}}{\partial \eta_2^2} & -\dfrac{\partial^2 \Phi^{\text{branch}}}{\partial \xi_2 \partial \eta_2} \\ & & -\dfrac{\partial^2 \Phi^{\text{branch}}}{\partial \xi_2 \partial \eta_2} & \dfrac{\partial^2 \Phi^{\text{branch}}}{\partial \xi_2^2} \end{bmatrix} [\mathbf{Q}_b] \tag{24}$$

Copyright © 2005 John Wiley & Sons, Ltd.

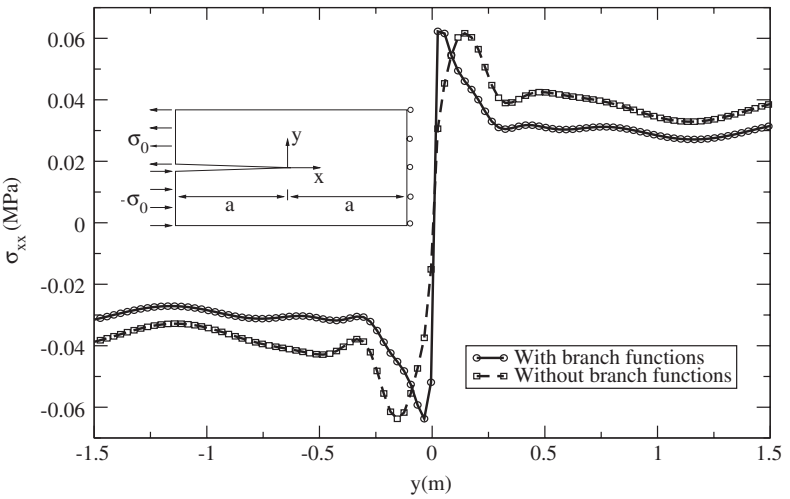

Figure 4. The stress σ_{xx} at $x = -0.3$ for a double cantilever beam to demonstrate the effect of the branched stress function.

where $[\mathbf{Q}_b]$ is the transformation matrix from (ξ_1, η_1) and (ξ_2, η_2) systems to (x, y), and is expressed as

$$[\mathbf{Q}_b] = \begin{bmatrix} \dfrac{\partial \eta_1}{\partial y} & \dfrac{\partial \eta_1}{\partial x} \\ \dfrac{\partial \xi_1}{\partial y} & \dfrac{\partial \xi_1}{\partial x} \\ \dfrac{\partial \eta_2}{\partial y} & \dfrac{\partial \eta_2}{\partial x} \\ \dfrac{\partial \xi_2}{\partial y} & \dfrac{\partial \xi_2}{\partial x} \end{bmatrix} \tag{25}$$

The branch function is evaluated at every integration point in the element. A typical function Φ^{branch} for $s = 0$ and $t = 0$ is plotted in Figure 3(b). The plot shows that the function is continuous everywhere in the domain except across the crack surface. The example of a double cantilever beam under a sliding load, as shown in Figure 4, explains the effect of level set method-based branch functions. In Figure 4, the dimension is $a = 1.5\,\text{m}$. Figure 4 shows the stress σ_{xx} plots as a function of y at $x = -0.3\,\text{m}$. The stress functions are constructed with and without branch functions in this example. σ_{xx} changes its sign with a jump in its magnitude on different sides of the crack and the jump at $y = 0$ is predicted well. However, the transition is gradual from negative to positive values for the curve without branch functions. Although the transition takes place in a short interval, the method is not able to catch the discontinuity without branch functions. This also results in the matrices $[\overset{1}{G}^{\text{cr}}]$ and $[\overset{2}{G}^{\text{cr}}]$ in Equation (16),

Copyright © 2005 John Wiley & Sons, Ltd.

on different sides of the crack to be linearly dependent on each other (one is the negative of the other).

3.3. Multi-resolution wavelet functions for modelling cohesive cracks

Wavelet bases, discussed in References [50, 51], are $L^2(\mathscr{R})$ and generally have compact support. Only the local coefficients in wavelet approximations are affected by abrupt changes in the solution, such as for shock waves. This localization property makes the wavelet basis a desirable tool for problems with a high solution gradients, concentrations or even singularity. A brief introduction to wavelet basis functions is provided next.

3.3.1. Principles of wavelets and multi-resolution analysis. The construction of wavelet functions starts from a scaling or dilatation function $\phi(x)$ and a set of related coefficients $\{p(k)\}_{k\in\mathscr{Z}}$ which satisfy the two-scale relation

$$\phi(x)=\sum_k p(k)\phi(2x-k) \tag{26}$$

The scaling function has a compact support only if many coefficients $p(k)$ are non-zero. Translations of the scaling function $\phi(x-k)$ form an unconditional basis of a subspace $V_0\subset L^2(\mathscr{R})$. Through a translation of ϕ by a factor of 2^n and dilation by a factor of $k\cdot 2^{-n}$ the unconditional basis is obtained for the subspace $V_n\subset L^2(\mathscr{R})$ as

$$\phi_{n,k}(x)=2^{n/2}\phi(2^n x-k) \tag{27}$$

for a resolution level n. The scaling function ϕ is defined as orthonormal if translations at the same level of resolution satisfies the condition

$$\int_{-\infty}^{\infty}\phi_{n,k}(x)\phi_{n,l}(x)\,\mathrm{d}x=\delta_{k,l}\quad\forall n,k,l\in\mathscr{Z} \tag{28}$$

Consequently, the best approximation of a function $f(x)$ in the subspace V_n of $L^2(\mathscr{R})$ is expressed as the orthogonal projection of f on V_n as

$$\mathscr{A}_n f(x)=\sum_k a_{n,k}\phi_{n,k}(x)\quad\text{where } a_{n,k}=\int_{-\infty}^{\infty}f(x)\phi_{n,k}(x)\,\mathrm{d}x \tag{29}$$

Approximation of $f(x)$, can be made at different resolution levels, and these approximations in subspaces $\ldots, V_{n-1}, V_n, V_{n+1}, \ldots,$ follow the relation

$$\{0\}=V_{-\infty}\subset\cdots\subset V_{-1}\subset V_0\subset V_1\subset\cdots\subset V_\infty=L^2(\mathscr{R})\quad\text{where}$$

$$\lim_{n\to\infty}V_n=\bigcup V_n\ \text{is dense in } L^2(\mathscr{R})\quad\text{and}\quad\lim_{n\to-\infty}\bigcap_n V_n=\{0\} \tag{30}$$

In the multi-resolution level transition, the information lost in the transition from level V_{n+1} to level V_n is characterized by an orthogonal complementary subspace W_n. A basis for the

Copyright © 2005 John Wiley & Sons, Ltd.

subspace W_n can be obtained is in the same manner as for scaling function, i.e. by dilating and translating the mother wavelet function

$$\psi(x) = \sum_k q(k)\psi(2x - k) \tag{31}$$

The subspaces spanned by the wavelet functions have the following essential properties:

(i) $V_{n+1} = V_n \oplus W_n \forall$, i.e. W_n is the orthogonal complement of V_n to V_{n+1}
(ii) For orthonormal bases, W_{n1} is orthogonal to W_{n2}
(iii) For orthonormal bases

$$\bigoplus_{n=-\infty}^{\infty} W_n = L^2(\mathscr{R}) \tag{32}$$

An approximation of the function $f(x)$ at the nth resolution level may be expressed as the orthogonal projection of f on W_n as

$$f \to \mathscr{D}_n f(x) = \sum_k b_{n,k}\psi_{n,k}(x) \quad \text{where } b_{n,k} = \int_{-\infty}^{\infty} f(x)\psi_{n,k}(x)\,\mathrm{d}x \tag{33}$$

Due to the orthonormality and multi-resolution properties of wavelet basis functions, higher level approximate solutions can be generated from results of lower level solutions (see References [50, 51]) by selective superposition of complementary solutions. The use of adaptive enrichment is very attractive to those regions where a pre-determined 'error or residual' tolerance is not met at the lower level.

3.3.2. Selection of the wavelet function. Various wavelet functions have been proposed in the literature for numerical solutions of ODEs and PDEs. These functions have been incorporated in the method of weighted residuals like the Galerkin's method and collocation method to solve problems with multi-level features in References [35–37]. Among the large number of wavelet functions proposed are the Haar function [52], the Meyer's wavelets [53], the Chui–Wang's B-spline wavelets [54], etc. One of the most commonly used wavelet functions is Daubechies' compactly supported orthonormal wavelets [35, 55, 56]. However, they are constructed through recursive algorithms and do not have an explicit analytic expressions. This makes it is difficult to obtain their first and second derivatives, which is a requirement in X-VCFEM for deriving stresses in terms of stress functions. Also the orthonormality of the Daubechies wavelet cannot be transferred to the orthonormality for stresses by differentiation, and hence they are not considered to be suitable for stress functions in X-VCFEM. Alternatively, a family of Gaussian functions, for which the first- and second-order derivatives are popular wavelets bases [57–59], is implemented in the representation of X-VCFEM stress functions and stresses. The expressions for the Gaussian function and its nth-order derivative are

$$G(x) = \mathrm{e}^{-((x-b)/a)^2/2} \quad \text{and} \quad \Psi_{a,b}^{G_n} = (-1)^n \frac{\mathrm{d}^n}{\mathrm{d}x^n}(\mathrm{e}^{-((x-b)/a)^2/2}) \tag{34}$$

The dilation and translation parameters a and b, respectively, can assume arbitrary values and can be changed in a continuous fashion. The ability of wavelets to translate diminishes the

Copyright © 2005 John Wiley & Sons, Ltd.

need to re-define new elements or remesh in conventional FEM solution of problems with moving boundaries. By changing translation parameters, the multi-levels of wavelet bases can be made to closely follow a moving crack tip. Additionally the dilation parameter with compact adjustable window support can be used to provide high refinement and resolution. Hence it is a convenient way of moving the stress concentrations using the multi-resolution properties.

3.3.3. Multiresolution wavelet-based stress functions for crack problems. The wavelet-based stress function is constructed in a local orthogonal coordinate system (ξ, η), centred at the crack tip. The ξ direction corresponds to the local tangent to the crack surface. The corresponding stress function $\Phi_{a,b,c,d}$ in the Gaussian wavelet basis is given as

$$\Phi_{a,b,c,d}(\xi, \eta) = \mathrm{e}^{-((\xi-b)/a)^2/2}\mathrm{e}^{-((\eta-d)/c)^2/2}\beta_{a,b,c,d} \tag{35}$$

where a, b, c, d are parameters that can take arbitrary continuous values. For implementation in multi-resolution analysis involving discrete levels, the translation and dilation parameters should be expressed as discrete multiples of some starting values. Consequently, these discrete values a_m, b_n, c_k and d_l are expressed as

$$\begin{aligned} a_m &= a_1 \cdot (\mathrm{tr}_a)^{m-1} \\ b_n &= n \cdot b_1 \cdot a_m \\ c_k &= c_1 \cdot (\mathrm{tr}_c)^{k-1} \\ d_l &= l \cdot d_1 \cdot c_k \end{aligned} \tag{36}$$

Here (m, k) correspond to the levels and (n, l) correspond to the discrete translation of the bases in the (ξ, η) directions, respectively. The parameters (a_1, c_1) are the initial dilating values at the first level $m = 1$, while $\mathrm{tr}_a (< 1), \mathrm{tr}_c (< 1)$ are the transfer rates from one level to the next higher one. The parameters b_1, d_1 represent the starting values of a step translation quantity at the mth dilation level. The narrow (higher level) wavelets are translated by small steps, whereas the wider (lower level) wavelets are translated by large steps. Parameters $\mathrm{tr}_a = \mathrm{tr}_c = 1$ and $b_1 = d_1 = 0$ imply no dilation and translation, respectively. Parameters c_0, c_c, and d_0 are counterparts of a_0, a_c, and b_0 in η direction. With the specific relations between dilation and translation parameters, the Gaussian wavelet enriched stress function in Equation (35) becomes

$$\Phi_{m,n,k,l}(\xi, \eta) = \mathrm{e}^{-((\xi-b_n)/a_m)^2/2}\mathrm{e}^{-((\eta-d_l)/c_k)^2/2}\beta_{m,n,k,l} \tag{37}$$

The family of wavelet-enriched stress functions in Equation (37) are not orthonormal, but they construct a linearly independent basis [60]. This leads to robustness and high precision in the reconstruction of any function f even with low-level coefficients. The wavelet enriched stress function in X-VCFEM is thus written as

$$\Phi^{\mathrm{wvlt}}(\xi, \eta) = \sum_{m=1,\, n=-n_n/2,\, k=1,\, l=0}^{m_n,\, n_n/2,\, k_n,\, l_n} \Phi_{m,n,k,l}(\xi, \eta) \tag{38}$$

Copyright © 2005 John Wiley & Sons, Ltd.

The corresponding stresses are

$$\begin{Bmatrix} \sigma_{\xi\xi} \\ \sigma_{\eta\eta} \\ \sigma_{\xi\eta} \end{Bmatrix} = \begin{Bmatrix} \dfrac{\partial^2 \Phi^{\text{wvlt}}}{\partial \eta^2} \\ \dfrac{\partial^2 \Phi^{\text{wvlt}}}{\partial \xi^2} \\ -\dfrac{\partial^2 \Phi^{\text{wvlt}}}{\partial \xi \partial \eta} \end{Bmatrix}$$

$$= \begin{Bmatrix} \displaystyle\sum_{m=1,\, n=-n_n/2,\, k=1,\, l=0}^{m_n,\, n_n/2,\, k_n,\, l_n} \dfrac{\partial^2 (\mathrm{e}^{-((\xi_1-b_n)/a_m)^2/2} \mathrm{e}^{-((\eta_1-d_l)/c_k)^2/2})}{\partial \eta^2} \beta_{m,n,k,l} \\ \displaystyle\sum_{m=1,\, n=-n_n/2,\, k=1,\, l=0}^{m_n,\, n_n/2,\, k_n,\, l_n} \dfrac{\partial^2 (\mathrm{e}^{-((\xi_1-b_n)/a_m)^2/2} \mathrm{e}^{-((\eta_1-d_l)/c_k)^2/2})}{\partial \xi^2} \beta_{m,n,k,l} \\ -\displaystyle\sum_{m=1,\, n=-n_n/2,\, k=1,\, l=0}^{m_n,\, n_n/2,\, k_n,\, l_n} \dfrac{\partial^2 (\mathrm{e}^{-((\xi_1-b_n)/a_m)^2/2} \mathrm{e}^{-((\eta_1-d_l)/c_k)^2/2})}{\partial \xi \partial \eta} \beta_{m,n,k,l} \end{Bmatrix} \tag{39}$$

The stress components in the global coordinate system are obtained by the transformation from the local coordinate system as

$$\begin{bmatrix} \sigma_{xx} & \sigma_{xy} \\ \sigma_{xy} & \sigma_{yy} \end{bmatrix}^{\text{wvlt}} = [\mathbf{Q}_w]^{\mathrm{T}} \begin{bmatrix} \dfrac{\partial^2 \Phi^{\text{wvlt}}}{\partial \eta^2} & -\dfrac{\partial^2 \Phi^{\text{wvlt}}}{\partial \xi \partial \eta} \\ -\dfrac{\partial^2 \Phi^{\text{wvlt}}}{\partial \xi \partial \eta} & \dfrac{\partial^2 \Phi^{\text{wvlt}}}{\partial \xi^2} \end{bmatrix} [\mathbf{Q}_w] \tag{40}$$

where $[\mathbf{Q}_w]$ is the transformation matrix from (ξ, η) to (x, y):

$$[\mathbf{Q}_w] = \begin{bmatrix} \dfrac{\partial \eta}{\partial y} & \dfrac{\partial \eta}{\partial x} \\ \dfrac{\partial \xi}{\partial y} & \dfrac{\partial \xi}{\partial x} \end{bmatrix} \tag{41}$$

Figure 5 shows the support region for the wavelets-enriched $\Phi^{\text{wvlt}}(\xi, \eta)$ in a X-VC element. This region is positioned symmetrically in the vicinity of evolving crack tips. The crosses ($\times$) corresponds to the position of each wavelet basis function b_n, d_n at a lower level, and the squares ($\square$) correspond to additional locations at a higher level in the multi-resolution algorithm. Only the points at the top half are shown in the figure due to symmetry.

The method of implementation of the multi-resolution wavelet-enriched stress functions in X-VCFEM is described below:

1. For the starting level $m = k = 1, 20$ points marked by crosses ($\times$) in Figure 5(a), are used to delineate the wavelet-enriched function $\Phi^{\text{wvlt}}(\xi, \eta)$ in Equation (38). This corresponds to $m = 1,\ n = 5,\ k = 1$ and $l = 4$.

Copyright © 2005 John Wiley & Sons, Ltd.

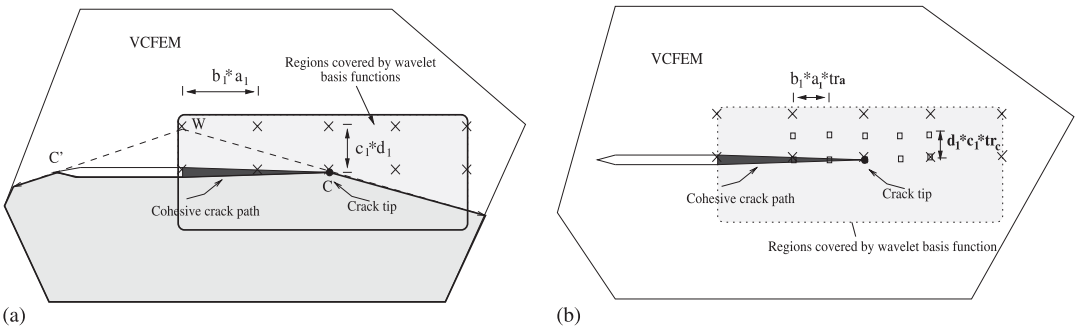

Figure 5. Distribution of multi-resolution wavelet bases around a crack tip: (a) crosses (×) refer to the location of the origin of the basis vectors at a lower level corresponding to dilation parameters (tr_a and tr_c); and (b) adaptively upgraded to higher level wavelet bases with the addition of the next level of bases at locations indicated by the squares (□).

2. With ensuing higher levels in the multi-resolution wavelet functions according to Equation (36), higher level wavelet bases are added to the stress function as marked by squares (□) in Figure 5(b). The addition is done adaptively in accordance with error criteria discussed in Section 3.4. A refinement in the starting region of wavelet enrichment occurs in each added level, i.e. the window size of additional wavelet basis functions is smaller than ones at a lower level. This allows a zoom in to catch higher gradients that are missed at the coarser scales.
3. The process of successive multi-level refinement can continue till a predetermined error tolerance is reached.

Remark

The line of the cohesive crack is likely to intersect the region of support of the wavelet bases functions. It is important for the numerical algorithms to assure that wavelet functions based on one side of the cohesive crack does not contribute to stresses on the other side. The influence of wavelet stress functions should be cut off across this line of discontinuity by establishing a truncated effective support domain for the wavelet function. This is accommodated by ignoring the contribution of quadrature points in the numerical integration on the other side of the crack as detailed in Section 5.2.1.

In summary, the stresses in an element are computed by adding contributions from Equations (20), (22) and (39), to yield

$$\begin{Bmatrix}\sigma_{xx}\\ \sigma_{yy}\\ \sigma_{xy}\end{Bmatrix}_e = \begin{Bmatrix}\sigma_{xx}\\ \sigma_{yy}\\ \sigma_{xy}\end{Bmatrix}_e^{\text{poly}} + \begin{Bmatrix}\sigma_{xx}\\ \sigma_{yy}\\ \sigma_{xy}\end{Bmatrix}_e^{\text{branch}} + \begin{Bmatrix}\sigma_{xx}\\ \sigma_{yy}\\ \sigma_{xy}\end{Bmatrix}_e^{\text{wvlt}}$$

$$= [[\mathbf{P}]^{\text{poly}} \quad [\mathbf{P}]^{\text{branch}} \quad [\mathbf{P}]^{\text{wvlt}}]_e \begin{Bmatrix}\beta_{pq}\\ \beta_{st}\\ \beta_{m,n,k,l}\end{Bmatrix}_e = [\mathbf{P}]_e\{\beta\}_e \tag{42}$$

Copyright © 2005 John Wiley & Sons, Ltd.

3.4. Error measure for adaptive wavelet enrichment

The Euler equation (3) indicates that the error in the kinematic equation, which is satisfied in a weak sense, may be primarily attributed to the lack of adequate resolution in the equilibrated stress fields. A strain energy-based element error measure, derived in Reference [30], is extended to the present problem. Let a stress field be enriched from a level n to $n+1$ by adding the wavelet-based enrichment stress $\boldsymbol{\sigma}^{\text{enr}}$, i.e.

$$\boldsymbol{\sigma}^{\text{level}(n+1)} = \boldsymbol{\sigma}^{\text{level}(n)} + \boldsymbol{\sigma}^{\text{enr}} \tag{43}$$

The corresponding percentage change in the strain energy ($\text{SE} = \int_{\Omega_{\text{enr}}} \sigma_{ij} S_{ijkl} \sigma_{kl} \, \mathrm{d}\Omega$), may be expressed as

$$\Delta\text{SE} = \frac{\text{SE}(\boldsymbol{\sigma}^{\text{level}:n+1}) - \text{SE}(\boldsymbol{\sigma}^{\text{level}:n})}{\text{SE}(\boldsymbol{\sigma}^{\text{level}:n+1})} \times 100\% \tag{44}$$

In view of the local properties of wavelets and stress concentration at crack tips, the strain energy in Equation (44) is calculated only in a small region around crack tip Ω_{enr}. Adding levels is conditioned upon the requirement that ΔSE is less than a preset tolerance, which in this paper is chosen to be $\approx 4\%$.

4. SOLUTION METHOD

Crack growth in multiple cracked materials is solved using an incremental approach, where a set of elemental and global equations are solved in each increment for stresses and displacements.

1. Local equations for each element are obtained by substituting the stress interpolations of Equation (42) and boundary/crack face displacement interpolations of Equation (14) in the element energy functional equation (16) and setting its variation with respect to the stress coefficients $\Delta\boldsymbol{\beta}$ to zero. This results in the weak form of the element kinematical relations

$$[\mathbf{H}]_e\{\boldsymbol{\beta} + \Delta\boldsymbol{\beta}\}_e = [[\mathbf{G}^e] \;\; [\overset{1}{\mathbf{G}}{}^{\text{cr}}] \;\; -[\overset{2}{\mathbf{G}}{}^{\text{cr}}]]_e \begin{Bmatrix} \mathbf{q}^e + \Delta\mathbf{q}^e \\ \overset{1}{\mathbf{q}}{}^{\text{cr}} + \Delta\overset{1}{\mathbf{q}}{}^{\text{cr}} \\ \overset{2}{\mathbf{q}}{}^{\text{cr}} + \Delta\overset{2}{\mathbf{q}}{}^{\text{cr}} \end{Bmatrix}_e \tag{45}$$

   or in a condensed form

$$[\mathbf{H}]_e\{\boldsymbol{\beta} + \Delta\boldsymbol{\beta}\}_e = [\mathbf{G}]_e\{\mathbf{q} + \Delta\mathbf{q}\}_e \tag{46}$$

   Since Equation (46) is linear, the stress coefficients can be directly expressed in terms of the nodal displacements, provided the element $[\mathbf{H}]_e$ matrix is invertible.
2. Subsequently, the weak forms of the global traction continuity conditions are solved by setting the variation of the total domain energy functional with respect to the generalized

Copyright © 2005 John Wiley & Sons, Ltd.

displacement components to zero. This results in the weak form of the traction reciprocity conditions

$$\sum_{e=1}^{N} [[\mathbf{G}^e] \ [\overset{1}{\mathbf{G}}{}^{\mathrm{cr}}] \ -[\overset{2}{\mathbf{G}}{}^{\mathrm{cr}}]]_e^{\mathrm{T}} \{\boldsymbol{\beta} + \Delta\boldsymbol{\beta}\}_e = \sum_{e=1}^{N} \begin{Bmatrix} \hat{\mathbf{t}} \\ \bar{\mathbf{f}}_{\mathrm{coh}} \\ -\bar{\mathbf{f}}_{\mathrm{coh}} \end{Bmatrix}_e \tag{47}$$

or in a condensed form:

$$\sum_{e=1}^{N} [\mathbf{G}]_e^{\mathrm{T}} \{\boldsymbol{\beta} + \Delta\boldsymbol{\beta}\}_e = \sum_{e=1}^{N} \{\bar{\mathbf{T}}_{\mathrm{ext}}\}_e \tag{48}$$

The forces at the crack surface are expressed in terms of the cohesive energy as

$$\bar{\mathbf{f}}_{\mathrm{coh}} = \int_{\Gamma_{\mathrm{cr}}} \frac{\partial}{\partial \Delta \overset{1}{\mathbf{q}}{}^{\mathrm{cr}}} \left[\int_{\overset{1}{\mathbf{u}}{}^{\mathrm{cr}} - \overset{2}{\mathbf{u}}{}^{\mathrm{cr}}}^{\overset{1}{\mathbf{u}}{}^{\mathrm{cr}} + \Delta\overset{1}{\mathbf{u}}{}^{\mathrm{cr}} - \overset{2}{\mathbf{u}}{}^{\mathrm{cr}} - \Delta\overset{2}{\mathbf{u}}{}^{\mathrm{cr}}} t_i^{\mathrm{coh}} d(\overset{1}{u}{}_i^{\mathrm{cr}} - \overset{2}{u}{}_i^{\mathrm{cr}}) \right] \mathrm{d}\Gamma_{\mathrm{cr}} \tag{49}$$

Combining Equations (46) and (48) and eliminating the stress coefficients $\{\boldsymbol{\beta} + \Delta\boldsymbol{\beta}\}_e$, results in the equation for solving the generalized displacements

$$\sum_{e=1}^{N} \{[\mathbf{G}]_e^{\mathrm{T}} [\mathbf{H}]_e^{-1} [\mathbf{G}]_e\} \{\mathbf{q} + \Delta\mathbf{q}\} = \sum_{e=1}^{N} \{\bar{\mathbf{T}}_{\mathrm{ext}}\}_e \tag{50}$$

Equation (50) is a non-linear matrix equation system due to the cohesive laws. Consequently, a Newton–Raphson iterative solver is invoked to solve for the increments of nodal displacements. The linearized form of Equation (50) for the *j*th iteration is

$$\left\{ \sum_{e=1}^{N} \frac{\partial \{\bar{\mathbf{T}}_{\mathrm{ext}}\}_e}{\partial \{\mathbf{q}\}} - \sum_{e=1}^{N} \{[\mathbf{G}]^{\mathrm{T}} [\mathbf{H}]^{-1} [\mathbf{G}]\}_e \right\}^j \{\mathrm{d}\mathbf{q}\}^j$$

$$= \left\{ \sum_{e=1}^{N} \{\bar{\mathbf{T}}_{\mathrm{ext}}\}_e - \sum_{e=1}^{N} \{[\mathbf{G}]^{\mathrm{T}} [\mathbf{H}]^{-1} [\mathbf{G}]\}_e \{\mathbf{q} + \Delta\mathbf{q}\} \right\}^j \tag{51}$$

which, in a condensed form is

$$[\mathbf{K}^g]^j \mathrm{d}\mathbf{q}^j = \{\mathbf{R}_{\mathrm{ext}}^g\} - \{\mathbf{R}_{\mathrm{int}}^g\}^j \tag{52}$$

A numerical problem associated with modelling cohesive crack growth is the occurrence of snap-back as is shown in the macroscopic load–deformation behaviour plot of Figure 6. This has been discussed for a three-point bending solution in Reference [27]. For a deformation-controlled process with monotonically changing deformation, the solution ignores the reverse portion of the displacement BCD, occurring with snap-back. The Newton–Raphson solver, where the loading process is monotonically controlled by incremental deformation or load conditions, exhibits a discontinuous drop from point B to D. It is obvious, that this solver needs to be augmented with the capability to account for the part BCD, i.e. to decrease both load and deformation with the growth

Copyright © 2005 John Wiley & Sons, Ltd.

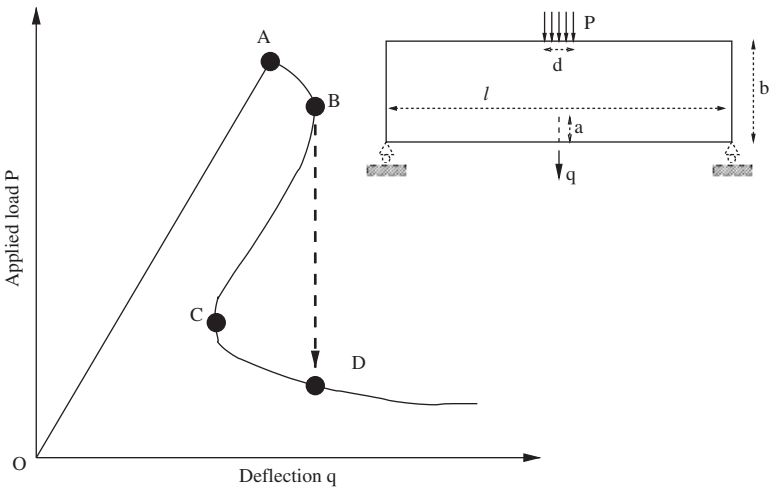

Figure 6. Load–deflection behaviour in a three-point bend test with a crack, showing the softening snap back phenomenon.

and opening of the crack. The arc-length solver has been proposed in References [61–63] as a method of overcoming this shortcoming by introducing an unknown loading parameter $(\lambda + \mathrm{d}\lambda)$ to govern the load increments. Equation (52) is modified with this loading parameter as

$$[\mathbf{K}^g]^j \mathrm{d}\mathbf{q}^j = (\lambda^j + \mathrm{d}\lambda^j)\{\mathbf{R}^g_{\mathrm{ext}}\} - \{\mathbf{R}^g_{\mathrm{int}}\}^j \tag{53}$$

where both $\mathrm{d}\lambda^j$ and $\mathrm{d}\mathbf{q}^j$ are unknowns, and $\mathrm{d}\lambda^j$ can be either positive or negative. The additional unknown $\mathrm{d}\lambda^j$ requires the solution of a constraint equation, written in terms of the magnitude of the deformation of all the nodes on the crack surface as

$$\sum_{i \in \mathrm{Crk}} ((\Delta \overset{1}{\mathbf{u}}{}^{\mathrm{cr}}_i)^2 + (\Delta \overset{2}{\mathbf{u}}{}^{\mathrm{cr}}_i)^2) = \Delta l^2 \tag{54}$$

where Crk represents the set of all nodes on crack surfaces. A summary of the solution process is explained in the flowchart of Figure 7.

5. ASPECTS OF NUMERICAL IMPLEMENTATION

5.1. Adaptive criteria for cohesive crack growth

A. Direction of incremental cohesive crack advance: In linear elastic fracture mechanics, it is common to use the 'maximum hoop stress criterion' to determine the direction of crack propagation [25, 47]. Cracks are assumed to propagate in a direction normal to the maximum hoop stress in this criterion. Since stresses at crack tip are singular in LEFM, stress intensity factors are usually used to determine the direction of crack propagation. This criterion is

Copyright © 2005 John Wiley & Sons, Ltd.

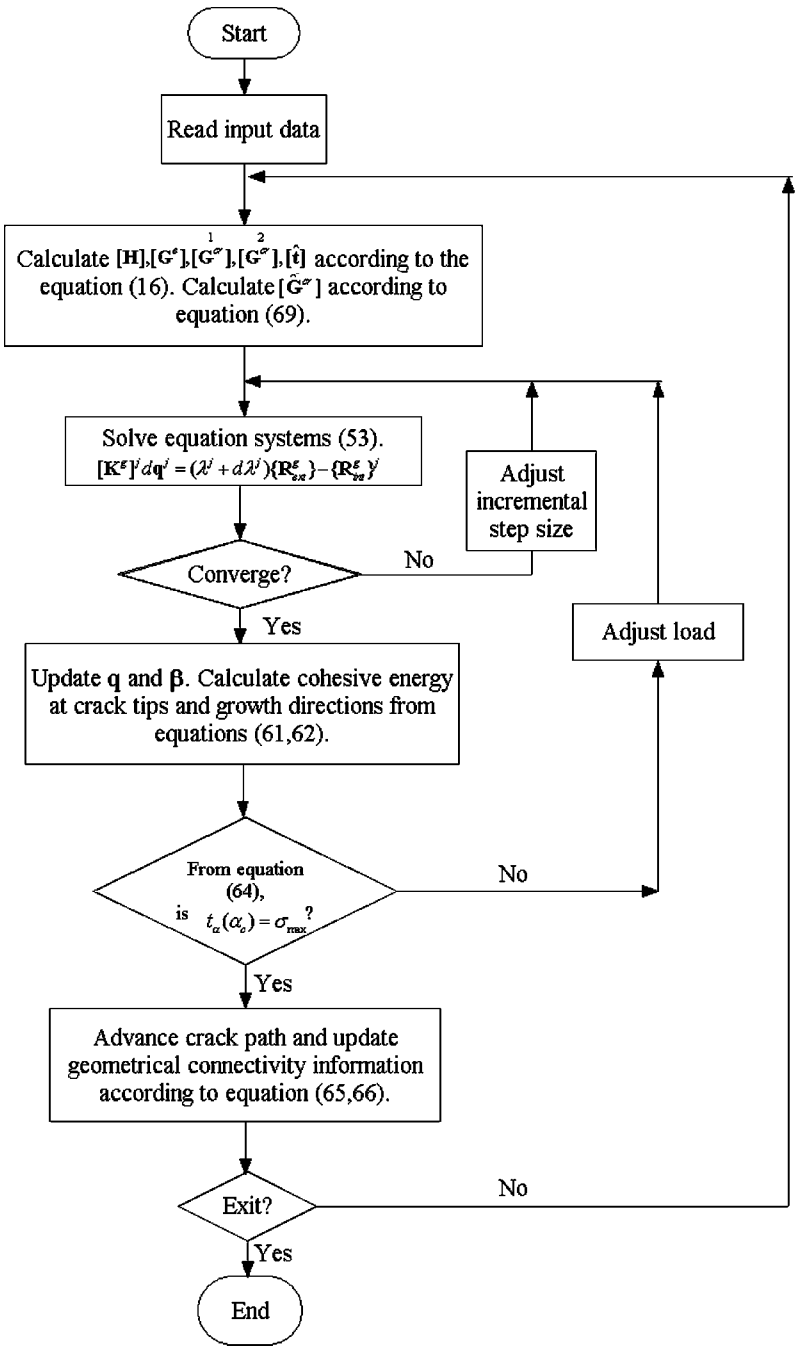

Figure 7. A flowchart of the solution method.

Copyright © 2005 John Wiley & Sons, Ltd.

only suitable for K-dominated problems, where the size of the fracture process zone is small compared to the size of the specimen. A different criterion, based on the cohesive energy at the crack tip is used in X-VCFEM. A relation between the cohesive energy ϕ for complete decohesion and the energy release rate G_c has been established in Reference [20] from the definition of the J-integral as

$$G_c = J = \int_0^R t \frac{\partial \delta}{\partial x_1} \, \mathrm{d}x_1 = \int_0^{\delta_e} t \, \mathrm{d}\delta = \phi \tag{55}$$

where R is the length of the cohesive zone. Consequently, the crack growth direction is estimated as that, along which G_c or equivalently the cohesive energy ϕ is maximized for a given crack-tip state of stress. The cohesive energy ϕ_A at the crack tip A along any direction α can be expressed for an arbitrary separation $\delta(\alpha)$ as

$$\phi_A(\alpha) = \left(\int_0^{\delta(\alpha)} t(\alpha) \, \mathrm{d}\delta \right)_A = \left(\int_{\sigma_{\max}}^{t(\alpha)} t(\alpha) \cdot \frac{\partial \delta}{\partial t} \, \mathrm{d}t \right)_A \tag{56}$$

where $t(\alpha) = \sqrt{(t_n^{\mathrm{coh}})^2 + \beta^{-2}(t_t^{\mathrm{coh}})^2}$ is the magnitudes of the effective cohesive force. The corresponding unit normal $\mathbf{n}$ and tangential $\mathbf{t}$ vectors along the direction α are expressed as

$$\mathbf{n} = -\sin\alpha \mathbf{i} + \cos\alpha \mathbf{j}, \quad \mathbf{t} = \cos\alpha \mathbf{i} + \sin\alpha \mathbf{j} \tag{57}$$

The normal and tangential components of the cohesive traction force at an angle α may then be deduced as

$$\begin{Bmatrix} t_n^{\mathrm{coh}} \\ t_t^{\mathrm{coh}} \end{Bmatrix} = \begin{bmatrix} n_x & n_y \\ t_x & t_y \end{bmatrix} \begin{Bmatrix} \sigma_{xx} n_x + \sigma_{xy} n_y \\ \sigma_{xy} n_x + \sigma_{yy} n_y \end{Bmatrix} = \begin{Bmatrix} \sigma_{xx} \sin^2\alpha - \sigma_{xy} \sin 2\alpha + \sigma_{yy} \cos^2\alpha \\ -\frac{1}{2}\sigma_{xx} \sin 2\alpha + \sigma_{xy} \cos 2\alpha + \frac{1}{2}\sigma_{yy} \sin 2\alpha \end{Bmatrix} \tag{58}$$

and hence the effective cohesive traction for direction α is

$$t(\alpha) = \sqrt{(\sigma_{xx} \sin^2\alpha - \sigma_{xy} \sin 2\alpha + \sigma_{yy} \cos^2\alpha)^2 + \beta^{-2}(-\tfrac{1}{2}\sigma_{xx} \sin 2\alpha + \sigma_{xy} \cos 2\alpha + \tfrac{1}{2}\sigma_{yy} \sin 2\alpha)^2} \tag{59}$$

The incremental direction of crack propagation is assumed as that which maximizes the cohesive energy at A, according to the criterion:

$$\frac{\partial \phi_A(\alpha)}{\partial \alpha} = 0 \quad \text{and} \quad \frac{\partial^2 \phi_A(\alpha)}{\partial \alpha^2} < 0 \tag{60}$$

A combination of Equations (56), (59) and (60), yield

$$\phi_A(\alpha) = \frac{\delta_e}{2\sigma_{\max}} (\sigma_{\max}^2 - t(\alpha)^2)$$

$$\frac{\partial \phi_A}{\partial \alpha} = -\frac{\delta_e}{\sigma_{\max}} t \frac{\partial t}{\partial \alpha} = 0 \Longrightarrow \tag{61a}$$

Copyright © 2005 John Wiley & Sons, Ltd.

$$\frac{\partial t}{\partial \alpha} = \frac{1}{\sqrt{(\sigma_{xx}\sin^2\alpha - \sigma_{xy}\sin 2\alpha + \sigma_{yy}\cos^2\alpha)^2 + \beta^{-2}(-\frac{1}{2}\sigma_{xx}\sin 2\alpha + \sigma_{xy}\cos 2\alpha + \frac{1}{2}\sigma_{yy}\sin 2\alpha)^2}}$$

$$\times[(\sigma_{xx}\sin^2\alpha - \sigma_{xy}\sin 2\alpha + \sigma_{yy}\cos^2\alpha)(\sigma_{xx}\sin 2\alpha - 2\sigma_{xy}\cos 2\alpha - \sigma_{yy}\sin 2\alpha)$$

$$+\beta^{-2}(-\tfrac{1}{2}\sigma_{xx}\sin 2\alpha + \sigma_{xy}\cos 2\alpha + \tfrac{1}{2}\sigma_{xx}\sin 2\alpha)(-\sigma_{xx}\cos 2\alpha - 2\sigma_{xy}\sin 2\alpha + \sigma_{yy}\cos 2\alpha)]$$

$$= 0 \tag{61b}$$

$$\frac{\partial^2 \phi_A}{\partial \alpha^2} = \frac{\delta_e}{\sigma_{\max}}[(\sigma_{xy}\sin 2\alpha - \sigma_{xx}\sin^2\alpha - \sigma_{yy}\cos^2\alpha)(\sigma_{xx}\sin 2\alpha - 2\sigma_{xy}\cos 2\alpha - \sigma_{yy}\sin 2\alpha)$$

$$+\beta^{-2}(\tfrac{1}{2}\sigma_{xx}\sin 2\alpha - \sigma_{xy}\cos 2\alpha - \tfrac{1}{2}\sigma_{yy}\sin 2\alpha)^2(-\sigma_{xx}\cos 2\alpha - 2\sigma_{xy}\sin 2\alpha + \sigma_{yy}\cos 2\alpha)]$$

$$< 0 \tag{61c}$$

Equation (61b) results from the fact that t cannot be equal to zero for decohesion to initiate and hence the necessary condition evolves from its derivative. The direction of crack propagation α_c is obtained as the solution of Equation (61b) as

$$\alpha_c^{\text{XVCFEM}} = \begin{cases} \arctan\left(\dfrac{-\sigma_{xx} + \sigma_{yy} \pm \sqrt{(\sigma_{xx} - \sigma_{yy})^2 + 4\sigma_{xy}^2}}{2\sigma_{xy}}\right) \\ \arctan\left(\dfrac{2(\beta^2 - 1)\sigma_{xy} \pm \sqrt{(4\beta^4 - 8\beta^2 + 4)\sigma_{xy}^2 - (4\beta^4 - 4\beta^2 + 2)\sigma_{xx}\sigma_{yy} - (2\beta^2 - 1)(\sigma_{xx}^2 + \sigma_{yy}^2)}}{2\beta^2\sigma_{xx} - \sigma_{xx} + \sigma_{yy}}\right) \end{cases} \tag{62}$$

The optimal angle α_c^{XVCFEM} is chosen as the one that satisfies the condition in Equation (61c). The corresponding angle given by the maximum hoop stress criterion in LEFM is expressed in terms of the stress intensity factors K_{I}, K_{II} as

$$\alpha_c^{\text{LEFM}} = 2\arctan\tfrac{1}{4}(K_{\text{I}}/K_{\text{II}} \pm \sqrt{(K_{\text{I}}/K_{\text{II}})^2 + 8}) \tag{63}$$

where the sign is chosen to make the hoop stress positive. The first of Equation (62), which is the only choice for $\beta = 1$, exactly matches the angle given by the maximum hoop stress criterion (63). For the pure sliding problem shown in Figure 4, α_c predicted by Equation (63) is 70.5°, while that by X-VCFEM for cohesive stresses is 68.2°. Along the direction α_c^{XVCFEM}, crack starts to propagate at

$$t_A(\alpha_c^{\text{XVCFEM}}) = \sigma_{\max} \tag{64}$$

Copyright © 2005 John Wiley & Sons, Ltd.

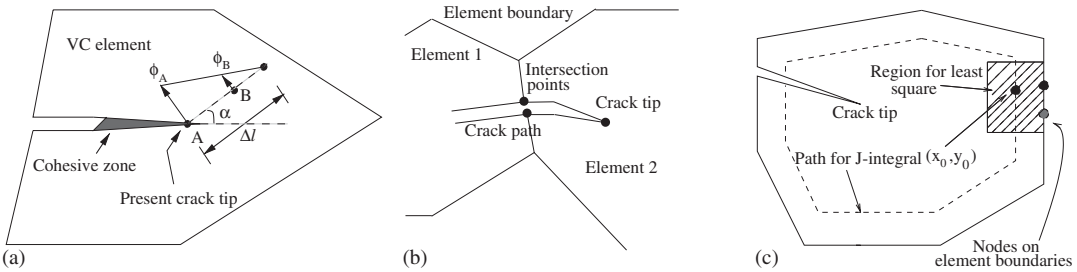

Figure 8. (a) Criteria for incremental propagation of cohesive cracks; (b) a cohesive crack going through the inter-element boundary; and (c) evaluation of J-integral.

B. Length of the incremental cohesive crack advance: Upon establishing the direction of incremental cohesive crack growth α_c, the length of cohesive zone advance ($\Delta\bar{l}$) should be estimated in the crack evolution scheme. The criterion used is that the cohesive energy goes zero at the end of the new segment as shown in Figure 8(a). To achieve this, the cohesive energy at two points A (present crack tip) and B (close to A in the direction of crack propagation) are evaluated by substituting the stresses in Equation (61a). The tip of the cohesive zone is obtained from the linear extrapolation of this line to yield zero cohesive energy. From Figure 8(a), the increment of cohesive crack length is defined as

$$\Delta\bar{l} = \frac{\phi_A}{\phi_A - \phi_B}|AB| \tag{65}$$

C. Cracks crossing the interelement boundaries: Crack advance from one Voronoi cell element to the next is conducted in X-VCFEM using an algorithm depicted in Figure 8(b). A continuous tracking method is implemented to monitor if a cohesive surface has reached or gone past an element boundary. In this method, the intersection of the crack surface and an element boundary is obtained by solving the equation system

$$\frac{x - x_i}{x_{i+1} - x_i} = \frac{y - y_i}{y_{i+1} - y_i}, \quad \frac{x - x_n}{x_{n+1} - x_n} = \frac{y - y_n}{y_{n+1} - y_n} \tag{66}$$

where (x_i, y_i) represents the tip of the cohesive crack line for the ith increment, and (x_n, y_n) is the position of the nth node on the element boundary. If the intersection point is outside of the cohesive line or the element boundary, no intersection is assumed. Once a cohesive crack has reached its intersection with the boundary, a new node pair $(n_1\ n_2)$ is introduced on the element boundary at this point. The node pair belongs to the intersection of the element boundary and the cohesive crack, i.e. $n_1 n_2 \in \partial\Omega_e^E \cap \Gamma_{\text{cr}}$. The crack is subsequently advanced to the next element following the usual procedure outlined before.

5.2. Numerical integration schemes for [**H**] *and* [**G**] *matrices*

5.2.1. Integration of [**H**] *matrix.* Numerical integration over each element is conducted by the Gaussian quadrature method to form the matrix [**H**] in Equation (17). In this method, each Voronoi cell element is recursively subdivided into triangular subdomains, on which, integration

Copyright © 2005 John Wiley & Sons, Ltd.

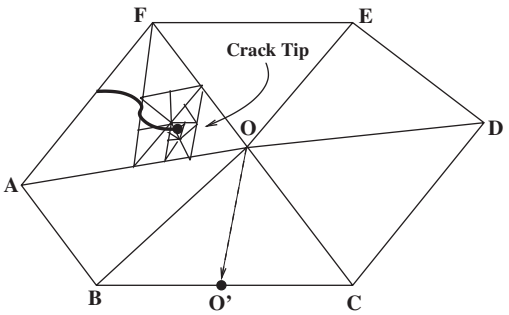

Figure 9. Subdivision of the Voronoi cell element for Gaussian quadrature, with a higher density of integration points near the crack tip.

points are generated for the Gaussian quadrature. The steps involved are discussed below:

1. For each Voronoi cell element shown in Figure 9, the centroid **O** is first generated. The first set of triangular subdomains is created by joining each of the vertices of the cell e.g. (**A**, **B**, **C**, **D**, **E**, **F**) with the centroid **O**.
2. Each triangle is further subdivided into two triangles if:

$$\frac{\text{Area of triangle}}{\text{Area of Voronoi cell element}} > \text{TOL}_{\text{area}}$$

   For the subdomain triangle **BCO** shown in Figure 9, two triangles are created by bisecting the longest edge **BC** at $\mathbf{O}'$ and joining it with the opposite vertex **O**. These new smaller triangles are again checked against the tolerance condition and further dissection is executed if necessary. Numerical integration in each triangular subdomain is done using 13 Gauss points.
3. For the region containing the crack tip shown in Figure 9, a smaller value of TOL_{area} is chosen in comparison with other regions. This facilitates a higher density of integration points in regions of high stress gradients. The tolerance in an element is consequently adjusted according to the distance of the centre of the triangular subdomain from the crack tip, i.e.

$$\text{TOL}_{\text{area}} = \text{TOL}_{\text{area}}^{\min} + \frac{(\text{TOL}_{\text{area}}^{\max} - \text{TOL}_{\text{area}}^{\min}) * d_{\text{tri}}}{L} \tag{67}$$

   where L is a scaling parameter defined in Section 3.1, d_{tri} is the distance of the crack tip from the subdomain and $\text{TOL}_{\text{area}}^{\max}$, $\text{TOL}_{\text{area}}^{\min}$ are assumed tolerances. In this work the tolerances are chosen as $\text{TOL}_{\text{area}}^{\max} = 10\%$ and $\text{TOL}_{\text{area}}^{\min} = 1\%$.
4. The intersection of the support of wavelet functions with the cohesive crack line call for a truncated support. This is done by eliminating the contribution of quadrature points that lie on the other side of crack face from the wavelet centre. A visibility criterion introduced in Reference [24] provides an easy way to accommodate this discontinuity in the construction of truncated support. In this method, the cracks are considered to be opaque when generating valid numerical integration regions. A ray is emitted from the

Copyright © 2005 John Wiley & Sons, Ltd.

center **W** of a wavelet basis function in an arbitrary direction as shown in Figure 5. If it encounters an internal crack, the ray is terminated. All quadrature points lying in the dark shadow region on the other side of the crack CC' are suppressed during numerical integration of this wavelet basis.

5.2.2. Integration of the [**G**] *matrices.* In Equation (17), the matrices $[\overset{1}{\mathbf{G}}^{\mathrm{cr}}]$ and $[\overset{2}{\mathbf{G}}^{\mathrm{cr}}]$ are numerically integrated over the crack surfaces and the matrix $[\mathbf{G}^e]$ over the element boundary. All numerical integrations on the element boundary and crack surfaces are executed using the Gaussian quadrature method. The number of integration points N_{int} on each boundary/crack-face segment depends on the distance d_{side} between its centre and the crack tip, and is chosen from the condition

$$N_{\mathrm{int}} = \begin{cases} 9, & d_{\mathrm{side}} \geqslant 0.1L \\ 16, & d_{\mathrm{side}} < 0.1L \end{cases} \tag{68}$$

where L is the scaling parameter.

5.3. Invertibility of the [**H**] *matrix*

A non-singular or invertible [**H**] matrix necessitates the linear independence of the columns of the [**P**] matrix. For pure polynomial expansions of the stress functions, this condition is naturally attained. However when adding the other terms, some of the terms in the branch and wavelet functions may have linear dependence on the polynomial terms. In X-VCFEM, the rank of the [**P**] matrix is first determined from the diagonal matrix resulting from a Cholesky factorization of the square matrix

$$[\mathbf{H}^*] = \int_{\Omega_e} [\mathbf{P}]^{\mathrm{T}} [\mathbf{P}] \, \mathrm{d}\Omega$$

Nearly dependent columns of [**P**] will result in very small pivots during Cholesky factorization. The corresponding branch and wavelet function terms are dropped from the stress function to prevent numerical inaccuracies in inverting [**H**].

5.4. Elimination of element rigid body modes

X-VCFEM uses a stress-based formulation with independent representation of displacement fields on the element and crack boundaries. In general, the nodes of the crack face are not topologically connected to the element boundary nodes. However it is important that all nodes in the element possess the same rigid body modes. The rigid body modes of the element boundary displacements $\{\mathbf{q}^e\}$ are directly constrained in the solution process through prescribed displacement boundary conditions. However, it is necessary to connect these with rigid-body modes for the crack face displacement fields $\{\overset{1}{\mathbf{q}}^{\mathrm{cr}}\}$ and $\{\overset{2}{\mathbf{q}}^{\mathrm{cr}}\}$. Singular value decomposition or SVD has been discussed in Reference [30] as an effective method for identifying and constraining rigid body modes at interfaces inside the Voronoi cell elements. The matrix product

Copyright © 2005 John Wiley & Sons, Ltd.

may be expressed as

$$[[\overset{1}{\mathbf{G}}^{\mathrm{cr}}] \quad -[\overset{2}{\mathbf{G}}^{\mathrm{cr}}]] \begin{Bmatrix} \overset{1}{\mathbf{q}}^{\mathrm{cr}} \\ \overset{2}{\mathbf{q}}^{\mathrm{cr}} \end{Bmatrix} = [\mathbf{U}][\boldsymbol{\lambda}][\mathbf{V}] \begin{Bmatrix} \overset{1}{\mathbf{q}}^{\mathrm{cr}} \\ \overset{2}{\mathbf{q}}^{\mathrm{cr}} \end{Bmatrix} = [\mathbf{U}][\boldsymbol{\lambda}] \begin{Bmatrix} \overset{1}{\hat{\mathbf{q}}}^{\mathrm{cr}} \\ \overset{2}{\hat{\mathbf{q}}}^{\mathrm{cr}} \end{Bmatrix}$$

$$= [[\overset{1}{\hat{\mathbf{G}}}^{\mathrm{cr}}] - [\overset{2}{\hat{\mathbf{G}}}^{\mathrm{cr}}]] \begin{Bmatrix} \overset{1}{\hat{\mathbf{q}}}^{\mathrm{cr}} \\ \overset{2}{\hat{\mathbf{q}}}^{\mathrm{cr}} \end{Bmatrix} \tag{69}$$

$[\mathbf{U}]$ and $[\mathbf{V}]$ are orthonormal matrices obtained by SVD of $[[\overset{1}{\mathbf{G}}^{\mathrm{cr}}] - [\overset{2}{\mathbf{G}}^{\mathrm{cr}}]]$. $[\boldsymbol{\lambda}]$ is a rectangular matrix with non-negative values on the diagonal. The zero or singular (very small values in numerical computations) values in $[\boldsymbol{\lambda}]$ corresponds to either trivial solutions or rigid body modes of the displacement solution. For accurate displacements, elements in $\{\hat{\mathbf{q}}^{\mathrm{cr}}\}$ corresponding to small or zero eigenvalues in $[\boldsymbol{\lambda}]$ are eliminated.

5.5. Evaluation of stress intensity factors

The stress intensity factors and *J*-integral are evaluated in the post-processing phase of the computations. From linear fracture mechanics, the relation between *J*-integral, stresses and stress intensity factors are given as

$$J = \int_{\Gamma} \left(\frac{1}{2} \sigma_{ik} \varepsilon_{ik} \delta_{1j} - \sigma_{ij} u_{i,1} \right) n_j \, \mathrm{d}s = \frac{K_{\mathrm{I}}^2}{E^*} + \frac{K_{\mathrm{II}}^2}{E^*} \tag{70}$$

where $E^* = E$ (Young's modulus) for plane stress, $E^* = E/(1 - \nu^2)$ for plane strain, and ν is the Poisson's ratio. In displacement-based FEM [27, 64], the contour integral is converted into a domain integral to improve the accuracy of the stress intensity factors, since the stresses are more accurate in the interior of an element. However in X-VCFEM, stresses on the contour and the interior are equally accurate due to stress interpolation and the contour integral can provide similar accuracy as the domain integral. A method to extract the stress intensity factors K_{I} and K_{II} from the *J*-integral, proposed in Reference [65], is implemented in X-VCFEM. Displacement fields are not interpolated in the interior of the Voronoi cell element, and hence the term $u_{2,1}$ in Equation (70) requires a special evaluation method.

1. Compute ε_{11}, ε_{22}, and ε_{12} at a series of points $(x_i, y_i,\ i = 1 \ldots N)$, in a small shadowed region around the integration point (x_0, y_0) in Figure 8(c). The displacement gradient $u_{1,1}$ is calculated from ε_{11}.
2. For evaluating $u_{2,1}$ displacements u_1 and u_2 at any point (x_i, y_i) are interpolated using polynomial functions,

$$\begin{aligned} u_1(x_i, y_i) &= a_0 + a_1 x_i + a_2 y_i + a_3 x_i^2 + \cdots \\ u_2(x_i, y_i) &= b_0 + b_1 x_i + b_2 y_i + b_3 x_i^2 + \cdots \end{aligned} \tag{71}$$

Copyright © 2005 John Wiley & Sons, Ltd.

where $a_0, a_1, \ldots, a_M$ and $b_0, b_1, \ldots, b_M$ are unknown coefficients. To constrain the rigid body motion, coefficients are evaluated from displacement values at two points on boundaries.

3. Displacement gradient expressions, $u_{1,1}(x_i, y_i)$, $u_{2,2}(x_i, y_i)$, $u_{1,2}(x_i, y_i)$ and $u_{2,1}(x_i, y_i)$ are obtained by taking derivatives of the expressions in Equation (71). Strain expressions in terms of the unknown coefficients are computed from these derivatives. At each point (x_i, y_i), the strains can also be computed from the known stresses and the compliance tensor, i.e. $\{\boldsymbol{\varepsilon}\} = [\mathbf{S}][\mathbf{P}]\{\boldsymbol{\beta}\}$. The unknown coefficients a_0, $a_1, \ldots, a_M$ and b_0, $b_1, \ldots, b_M$ in Equation (71) are estimated by solving a least square minimization problem for the strains. Subsequently the displacement gradient $u_{2,1}$ is determined at the integration point (x_0, y_0).

6. NUMERICAL EXAMPLES

The numerical examples solved, are divided into two categories. In the first set of examples, the convergence of X-VCFEM enriched by multi-resolution wavelet functions is demonstrated for static cracks by comparison with theoretical predictions and results available in the literature. The second set of examples show the effectiveness of X-VCFEM in modelling the propagation of multiple cohesive cracks.

6.1. Convergence tests for X-VCFEM for static cracks

6.1.1. Effects of translation and dilation parameters. Figure 10(a) shows a centre-cracked plate of width $2\mathbf{w} = 4\,\mathrm{m}$ and length $\mathbf{b} = 12\,\mathrm{m}$ with a crack length of $2\mathbf{a} = 1.6\,\mathrm{m}$. The plate is loaded in simple tension with a constant remote load of $\boldsymbol{\sigma} = 5\,\mathrm{MPa}$. The material parameters are: Young's modulus $E = 1\,\mathrm{MPa}$ and Poisson ratio $v = 0.3$. Due to problem symmetry, only the right half of the plate is modelled with one X-VCFEM element, as shown in Figure 10(b). Symmetry conditions are imposed on the left edge. The crack face is modelled using 10 node-pairs and the element boundary consists of 22 segments. The stress function used in this example consists of the three parts discussed in Section 3. For the polynomial function, the order of interpolation in Equation (18) corresponds to $p_n = 13$ and $q_n = 13$ for a total of 102 terms. For the branch function in Equation (22) consists of only 1 term with $s_n = 0$ and $t_n = 0$. The wavelet functions are changed from a lower level to a higher level using the adaptation criterion discussed in Section 3.4. Similar parameters are assumed for the ξ_1 and η_1 directions, i.e. $a_1 = c_1$, $\mathrm{tr}_a = \mathrm{tr}_c$ and $b_1 = d_1$ in Equation (36). The starting values of the parameters for the lower level ($m = k = 1$) are: $-2 \leqslant n \leqslant 3$, $0 \leqslant l \leqslant 1$, and $a_1 = c_1 = 0.1$. The result of X-VCFEM for this problem is plotted in terms of the stress σ_{yy} along the crack face ($y = 0$) as a function of the distance from the centre of the crack in Figure 11. Figure 11(a) corresponds to the stresses by varying the translation parameter b_1, while Figure 11(b) is for the variation of the dilation parameter a_1. From Figure 11(a) it is evident that a smaller b_1 make the stress concentration at the crack- tip higher. However, very small $b_1 \leqslant 0.001$ (no translation) leads to linear dependence of the columns of the [**P**] matrix generated from the wavelet basis functions, and should be avoided. Figure 11(b) shows that smaller a_1 results in faster convergence to higher crack-tip stress concentration. However, very small values of a_1 can also lead to oscillatory stresses. On the other hand, large a_1 values (≈ 0.15) shifts

Copyright © 2005 John Wiley & Sons, Ltd.

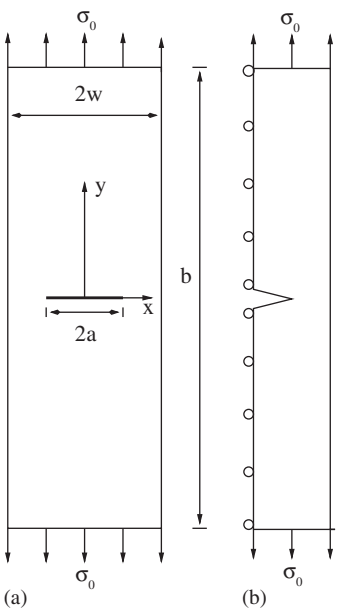

Figure 10. (a) A centre-cracked plate loaded in tension; and (b) a single X-VCFEM element with prescribed boundary conditions.

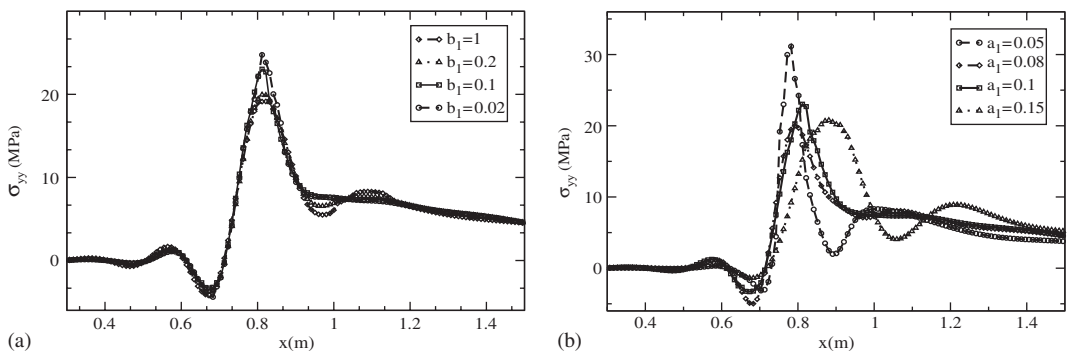

Figure 11. X-VCFEM generated stress σ_{yy} at $y = 0$ for the cracked plate, to examine the effect of parameters in the wavelet basis: (a) dilation parameters; and (b) translation parameters.

the stress peak. The optimal selection of these parameters is therefore very important. This is obtained through the multi-resolution construction of bases, discussed next.

The multi-resolution wavelet bases are significantly more effective in simulating crack problems. Table I shows the effect of the dilation transfer rate $\mathrm{tr}_a = \mathrm{tr}_c$ on the stress intensity factors for variation in the translation parameters $b_1 = d_1$. Other parameters in the simulation are $a_1 = c_1 = 0.1$, $m_n = k_n = 3$, $n_n = 6$, and $l_n = 2$. The values $\mathrm{tr}_a = \mathrm{tr}_c = 1$ imply no dilation.

Copyright © 2005 John Wiley & Sons, Ltd.

Table I. Normalized stress intensity factors (K_I/K_{ref}) for different values of tr_a and b_1 in the multi-resolution wavelet representation.

tr_a, b_1,	0.6, 0.05	0.6, 0.1	0.6, 0.2	0.5, 0.05	0.5, 0.1	0.5, 0.2	0.4, 0.05	0.4, 0.1	0.4, 0.2
K_I/K_{ref}	1.019	1.014	1.040	1.017	1.014	1.027	1.020	1.020	1.035

Table II. Errors with varying enrichment order of multi-resolution wavelet functions for the different cases.

	Case 1	Case 2	Case 3	Case 4	Case 5
$m_n = k_n$	0	1	2	3	4
K_I/K_{ref}	1.1642	1.0361	1.0208	1.0062	1.0020
ΔSE (%)		96.45	45.91	7.06	3.01

As tr_a approaches 1, the different levels functions become more and more dependent on each other. From the table, the minimum error is achieved for $b_1 = 0.1$ and $tr_a = tr_c = 0.5$ or 0.6.

6.1.2. Convergence with multi-resolution wavelet bases. The example in Section 6.1.1 is considered again for studying the solution convergence behaviour with multi-resolution wavelet functions. The four sets of parameters represent four instances of multi-resolution stress function enrichment. The first case consists of only polynomial and branch functions for the stress interpolation, for which the details are provided in Section 6.1.1. Cases 2–5, introduce different levels of the wavelet basis functions. The wavelet parameters common to these four cases are: $n_n = 6$, $l_n = 2$, $a_1 = c_1 = b_1 = d_1 = 0.1$, and $tr_a = tr_c = 0.5$. The parameters corresponding to the levels of the multi-resolution enrichment ($m_n = k_n$) are listed in Table II.

The mode I stress intensity factor is calculated for all the five cases and is normalized with respect to the analytical prediction K_{ref} by linear elastic fracture mechanics (LEFM), reported in Reference [66]. The second row of Table II compares this value for the different cases. Without the wavelet bases (case 1), the solution is 16% higher than the theoretical value. Cases 2–5 results demonstrate that the wavelet basis effectively reduces the error with increasing resolution level (m_n). The X-VCFEM generated stress σ_{yy} at $y = 0$ is plotted in Figure 12 for cases 1–4. Without the wavelet enrichment, the stress concentration at the crack tip ($x = 0.8$) is completely misrepresented. The stress peaks are represented with increasing accuracy with additional levels of multi-resolution wavelet functions. The strain energy error in Equation (44) is also calculated for cases 2–5 and tabulated in Table II. The error rapidly decreases with increasing wavelet enrichment, confirming the fast convergence rate of the multi-resolution algorithm. However, the stress intensity factor K_I is calculated from a contour that is away from the crack tip. The stresses on this contour are much more stabilized and additional wavelet bases do not affect these stresses considerably. Hence, the error in K_I is not significantly affected by their addition. From the above convergence tests, the optimal parameters for stress function representations in X-VCFEM are chosen to be $p_n = q_n = 13$, $s_n = t_n = 0$, $n_n = 6$, $l_n = 1$, $m_n = k_n = 4$, $a_1 = c_1 = b_1 = d_1 = 0.1$ and $tr_a = tr_c = 0.5$. These are retained for all subsequent simulations.

Copyright © 2005 John Wiley & Sons, Ltd.

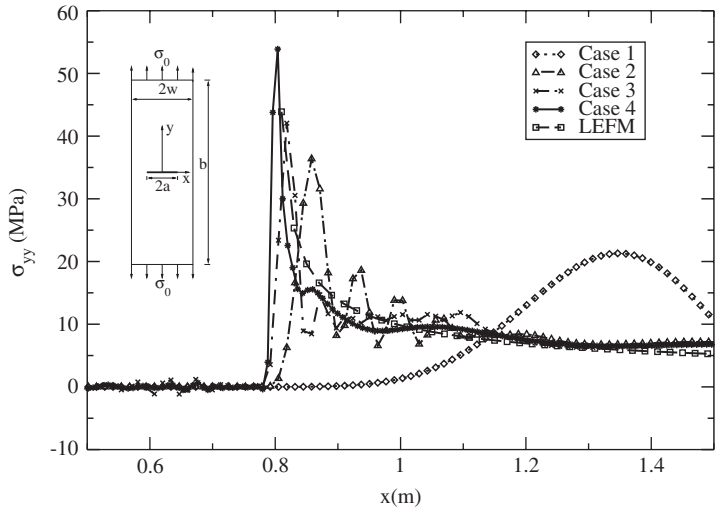

Figure 12. X-VCFEM generated stress σ_{yy} at $y = 0$ for different enrichment orders of the wavelet basis functions.

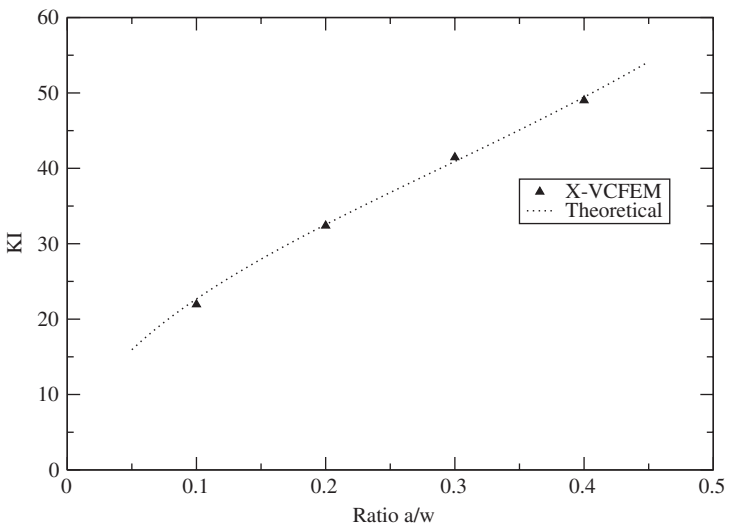

Figure 13. Stress intensity factors for various values of $\mathbf{a}/\mathbf{w}$.

X-VCFEM simulations of the cracked plate are further conducted for different crack lengths, to study the effect of this length on the solution convergence. The specific dimensions in Figure 10(a) are $2\mathbf{w} = 2\,\mathrm{m}$, $\mathbf{b} = 6\,\mathrm{m}$, while the crack length $2\mathbf{a}$ is varied. The plate is loaded under remote tension of $\boldsymbol{\sigma} = 40\,\mathrm{Pa}$. X-VCFEM solution of K_I for various values of $\mathbf{a}/\mathbf{w}$ are plotted in Figure 13 and compared with the theoretical predictions of Reference [66]. X-VCFEM predictions match the theoretical results extremely well.

Copyright © 2005 John Wiley & Sons, Ltd.

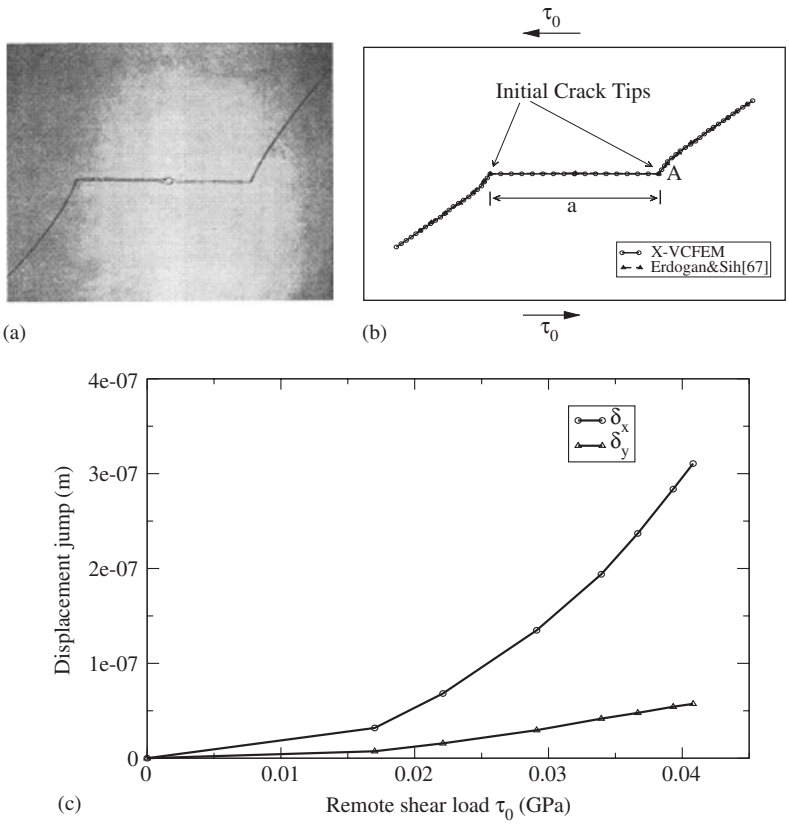

Figure 14. (a) Optical micrograph showing the path of cracking in a plate with a central crack subjected to far-field shear [67]; (b) corresponding crack path generated by X-VCFEM; and (c) crack opening displacement at the tip A.

6.2. Crack propagation in sheared plate with a central crack

This example is based on a classical problem of a single crack propagation in a large plate with a central crack. The plate is subjected to a far field shear load. The problem was experimentally studied by Erdogan and Sih [67] and an optical micrograph of their cracked specimen is shown in Figure 14(a). The specimen material in their experiment were assumed to be homogeneous, isotropic and linearly elastic and the crack was assumed to be brittle. A single element of dimension $10\,\text{m} \times 8\,\text{m}$ in X-VCFEM is used to simulate this experiment as shown in Figure 14(b). The initial crack length is $\mathbf{a} = 1.6\,\text{m}$. The material parameters are: Young's modulus $E = 100\,\text{GPa}$, Poisson ratio $\nu = 0.3$ and the cohesive law parameters are: $\sigma_{\max} = 0.1\,\text{MPa}$, $\beta = 1$, and $\delta_e = 1 \times 10^{-7}\,\text{m}$. The shear stress applied on the top and bottom surfaces, is varied from 0 to 0.041 GPa with plane stress assumptions. As shown in Figure 14(b), the crack path predicted by X-VCFEM compares well with the observations in Reference [67]. Figure 14(c) shows the growth of the crack opening displacement components at the right tip A. The entire computational process took 20 min on a single CPU in the Pentium 4 cluster with 2.4 GHz intel P4 Xeon processors.

Copyright © 2005 John Wiley & Sons, Ltd.

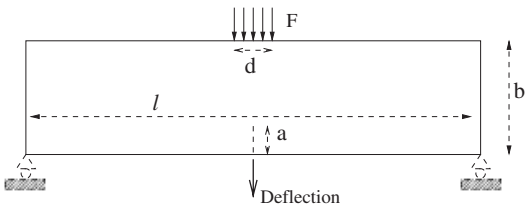

Figure 15. A three-point symmetric bending specimen.

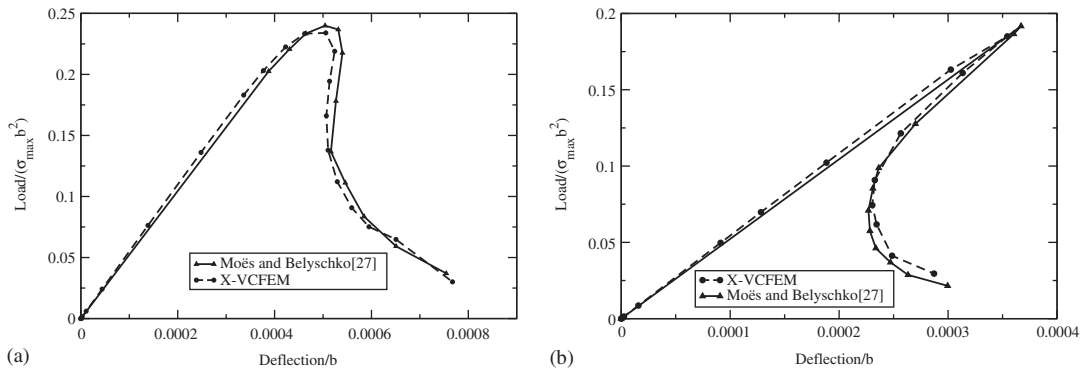

Figure 16. Comparison of normalized load–deflection curves for the three-point bending beam: (a) $\delta_e = 3.134796 \times 10^{-5}$ m; and (b) $\delta_e = 6.26959 \times 10^{-6}$ m.

6.3. Crack propagation in three-point bending specimen

Two numerical examples are considered for this specimen. In the first example, symmetric mode I crack propagation in a three-point bending test, as shown in Figure 15, is modelled. Plane stress conditions are assumed in the simulation. This problem of cohesive crack propagation has been studied by Carpinteri and Colombo [68] using node release technique and by Moës and Belytschko [27] using the XFEM. The geometrical dimensions for the specimen in Figure 15 are $\mathbf{b} = 0.15$ m, $\mathbf{l} = 4\mathbf{b}$, $\mathbf{t}$(specimen thickness) $= \mathbf{b}$, $\mathbf{a} = 0$, and $\mathbf{d} = 0.001$ m. The material properties are: Young's modulus $E = 36\,500$ MPa, Poisson ratio $v = 0.1$, and the cohesive parameters are $\sigma_{\max} = 3.19$ MPa, and $\beta = 0$. The X-VCFEM solution is compared with that in Reference [27] through the load–deflection curve of Figure 16. The cohesive displacement parameters are $\delta_e = 3.134796 \times 10^{-5}$ and 6.26959×10^{-6} m for Figures 16(a) and (b), respectively. A sharper snap-back is seen for the latter case. Excellent match is observed between the X-VCFEM and XFEM results.

The second example is that of a mixed-mode cohesive crack propagation in a three-point bend test due to an unsymmetrically positioned initial crack. The configuration, as shown in Figure 17(a), has been studied by Mariani and Perego [69] using XFEM under plane stress conditions. The initial crack position is determined by the offset ratio α, defined as the ratio of the distance of the initial crack from the mid-span cross-section to half of the beam span. The material Young's modulus $E = 31\,370$ MPa, and Poisson ratio $v = 0.2$. The cohesive model

Copyright © 2005 John Wiley & Sons, Ltd.

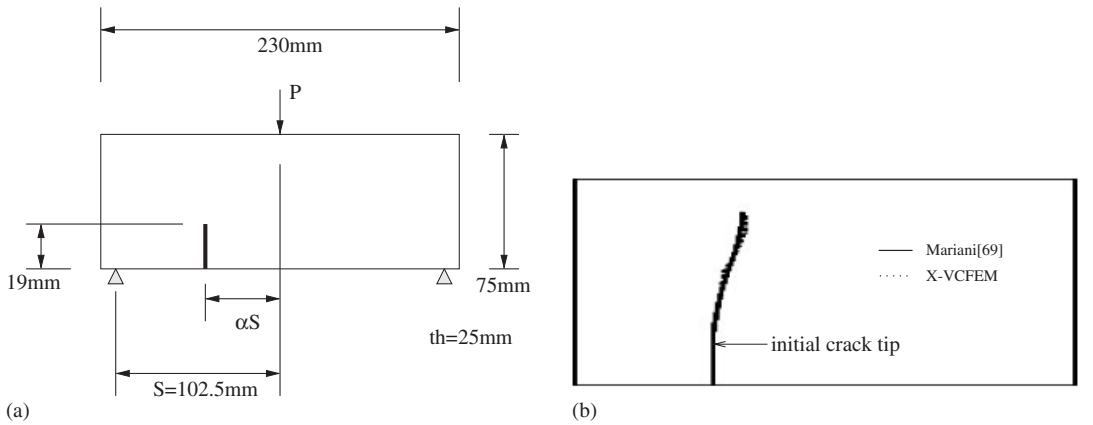

Figure 17. (a) A three-point bending specimen with an unsymmetric initial crack; and (b) comparison of the crack paths by X-VCFEM with that in Reference [69] for ($\alpha = 0.5$).

parameters are $\sigma_{\max} = 4.4\,\text{MPa}$, $\delta_{\max} = 0.07719298\,\text{mm}$ and $\beta = 1.0$. Again, the entire domain is represented by a single element in X-VCEFM. For $\alpha = 0.5$, the path of crack propagation is shown in Figure 17(b). The dashed and solid lines represent results from X-VCFEM and Reference [69], respectively. The results almost overlap, thus proving the effectiveness of X-VCFEM.

6.4. Mesh independence of crack propagation with X-VCFEM

A panel with domain $5\,\text{cm} \times 3\,\text{cm}$ containing two initial cracks is remotely loaded in tension as shown in Figure 18(a). The problem has been solved by Sharma *et al.* [70] using the element-free Galerkin meshless method. For X-VCFEM solution, the domain is meshed into two elements with three different topologies shown in Figure 18. Plane stress conditions are again assumed. A total of 11 increments is used to model the entire crack propagation process. The material parameters are: Young's modulus $E = 207\,\text{GPa}$ and Poisson ratio $v = 0.3$ and cohesive zone parameters are: $\sigma_{\max} = 0.1\,\text{MPa}$, $\delta_e = 1 \times 10^{-6}\,\text{cm}$, and $\beta = 1$. Figures 18(b)–(d) show no mesh dependence of the X-VCFEM predictions and the comparison with results in Reference [70] is excellent.

6.5. Propagation of randomly located multiple cracks

As a final example, a plate with five randomly located cracks is simulated under a tensile loading as shown in Figure 19(a). The plate has dimensions $0.6\,\text{m} \times 0.4\,\text{m}$; material parameters: Young's modulus $E = 10^5\,\text{MPa}$ and Poisson ratio $v = 0.3$; and cohesive parameters: $\sigma_{\max} = 0.1\,\text{MPa}$, $\beta = 1$, and $\delta_e = 1 \times 10^{-5}\,\text{cm}$. Figure 19(b) shows the final positions of the cracks that have grown with the loading. The cracks propagate across element boundaries and are attracted to each other in certain regions till they nearly merge.

Copyright © 2005 John Wiley & Sons, Ltd.

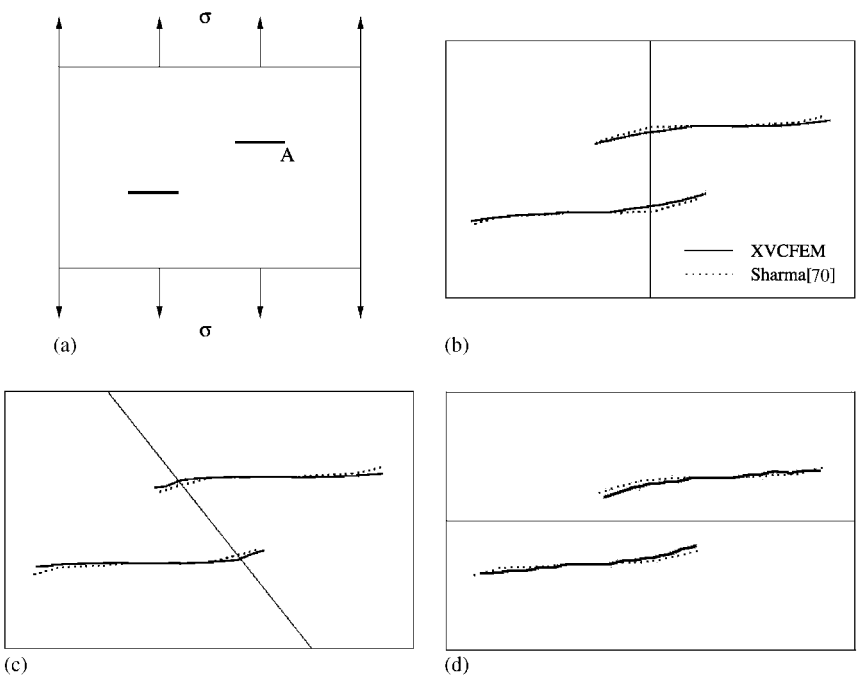

Figure 18. (a) A plate with two cracks in arbitrary locations modelled by X-VCFEM using elements of different topologies located cracks, (b–d) show crack path at the end of the loading for the different elements and also a comparison with Reference [70].

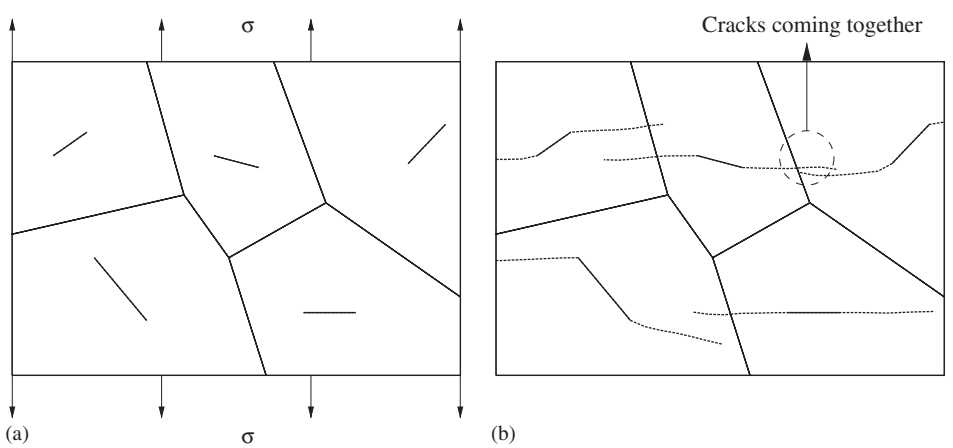

Figure 19. (a) X-VCFEM mesh for a plate with five randomly located cracks; and (b) crack paths at the end of loading.

Copyright © 2005 John Wiley & Sons, Ltd.

7. CONCLUDING REMARKS

The assumed stress-based Voronoi cell finite element model has been developed by the second author and his research group for accurate and efficient micromechanical modelling of heterogeneous materials. The method essentially has the same effect as the meshless method, since it does not need any further discretization of the Voronoi cell, which represents the immediate neighbourhood of a heterogeneity. In this paper, this element is enhanced in the form of an extended VCFEM or X-VCFEM to accurately and efficiently model propagation and growth of multiple cohesive cracks in a monolithic medium. The cracks are modelled by a linear cohesive zone model and their incremental directions and growth lengths are determined in terms of the cohesive energy near the crack tip. Important enhancements are made to the element to allow stress discontinuities across the cohesive crack and to accurately depict the crack-tip stress concentrations. These features are accommodated through the incorporation of (a) branch functions in conjunction with level set methods across crack contours, and (b) adaptive multi-resolution wavelet functions in the vicinity of the crack tip. Conditions and methods of stability are enforced in X-VCFEM for improved convergence with propagating cracks. Among the methods for improving convergence are the singular value decomposition in the construction of the stiffness matrices and the arc-length method in the solution process. Two classes of problems are solved and compared with existing solutions in the literature for validation of the X-VCFEM algorithms. The first set corresponds to results for static cracks, while in the latter set, the propagation of cohesive cracks are considered. The X-VCFEM results show excellent accuracy in their comparison with analytical and other numerical solutions.

The fact that X-VCFEM can provide sufficiently accurate and mesh-independent results of crack propagation with optimal efficiency, establishes its potential in the micromechanical fracture analysis of more complex heterogeneous domains. As a matter of fact, the current undertaking with X-VCFEM is the modelling of the entire microstructural failure process in reinforced microstructures. This involves crack initiation by particle/fibre cracking or interfacial debonding, crack branching and bridging through their propagation as discussed in this paper. The ultimate use of this method is in the multi-scale representation of failure in heterogeneous materials.

ACKNOWLEDGEMENTS

This work has been partially supported by the Air Force Office of Scientific Research through grant No. F49620-98-1-01-93 (Program Director: Dr B. L. Lee) and by the Army Research Office through grant No. DAAD19-02-1-0428 (Program Director: Dr B. Lamattina). This sponsorship is gratefully acknowledged. Computer support by the Ohio Supercomputer Center through grant PAS813-2 is also gratefully acknowledged.

REFERENCES

1. Yamamoto Y, Tokuda N. Determination of stress intensity factor in cracked plates by the finite element method. *International Journal for Numerical Methods in Engineering* 1973; **6**:427–439.
2. Yagawa Y, Aizawa T, Ando Y. Crack analysis of power hardening materials using a penalty function and superposition method. *Proceedings of the 12th Conference on Fracture Mechanics*, *ASTM STP*, vol. 700, 1980; 439–452.
3. Barsoum RS. On the use of isoparametric finite elements in linear fracture mechanics. *International Journal for Numerical Methods in Engineering* 1976; **10**:25–37.

Copyright © 2005 John Wiley & Sons, Ltd.

4. Barsoum RS. Triangular quarter-point elements as elastic and perfectly-plastic crack tip elements. *International Journal for Numerical Methods in Engineering* 1977; **11**:85–98.
5. Henshell RD, Shaw KG. Crack tip finite elements are unnecessary. *International Journal for Numerical Methods in Engineering* 1975; **9**:495–507.
6. Hibbit HD. Some properties of singular isoparametric element. *International Journal for Numerical Methods in Engineering* 1977; **11**:180–184.
7. Tong P, Pian THH, Lasry SJ. A hybrid-element approach to crack problems in plane elasticity. *International Journal for Numerical Methods in Engineering* 1973; **7**:297–308.
8. Tong P. A hybrid crack element for rectilinear anisotropic material. *International Journal for Numerical Methods in Engineering* 1977; **11**:377–403.
9. Lin KY, Tong P. Singular finite elements for the fracture analysis of v-notched plate. *International Journal for Numerical Methods in Engineering* 1980; **15**:1343–1354.
10. Piltner R. Special finite elements with holes and internal cracks. *International Journal for Numerical Methods in Engineering* 1985; **21**:1471–1485.
11. Jirousek SJ. Hybrid Treffz plate bending elements with p-method capabilities. *International Journal for Numerical Methods in Engineering* 1987; **24**:1367–1393.
12. Zeng D, Katsube N, Zhang J, Soboyejo W. Hybrid crack-tip element and its applications. *Finite Element in Analysis and Design* 2002; **38**:319–335.
13. Needleman A. A continuum model for void nucleation by interfacial debonding. *Journal of Applied Mechanics* 1987; **54**:525–531.
14. Needleman A. An analysis of decohesion along an imperfect interface. *International Journal of Fracture* 1990; **42**:21–40.
15. Needleman A. Micromechanical modelling of interfacial decohesion. *Ultramicroscopy* 1992; **40**:203–214.
16. Tvergaard V. Effect of fibre debonding in a whisker-reinforced metal. *Materials Science and Engineering* 1990; **A125**:203–213.
17. Foulk JW, Allen DH, Helms KLE. Formulation of a three-dimensional cohesive zone model for application to a finite element algorithm. *Computer Methods in Applied Mechanics and Engineering* 2000; **183**:51–66.
18. Geubelle PH. Finite deformation effects in homogeneous and interfacial fracture. *International Journal of Solids and Structures* 1995; **32**:1003–1016.
19. Camacho GT, Ortiz M. Computational modelling of impact damage in brittle materials. *International Journal of Solids and Structures* 1996; **33**:2899–2938.
20. Ortiz M, Pandolfi A. Finite-deformation irreversible cohesive element for three-dimensional crack-propagation analysis. *International Journal for Numerical Methods in Engineering* 1999; **44**:1267–1282.
21. Carpinteri A. Finite deformation effects in homogeneous and interfacial fracture. *Engineering Fracture Mechanics* 1989; **32**:265–278.
22. Xu XP, Needleman A. Finite deformation effects in homogeneous and interfacial fracture. *Journal of Mechanics and Physics of Solids* 1994; **42**(9):1397–1434.
23. Jirasek M. A comparative study on finite elements with embedded discontinuities. *Computer Methods in Applied Mechanics and Engineering* 2000; **188**(1):307–330.
24. Belytschko T, Krongauz Y, Organ D, Fleming M, Krysl P. Meshless methods: an overview and recent developments. *Computer Methods in Applied Mechanics and Engineering* 1996; **139**:3–47.
25. Belytschko T, Black T. Elastic crack growth in finite elements with minimal remeshing. *International Journal for Numerical Methods in Engineering* 1999; **45**(5):601–620.
26. Belytschko T, Organ D, Gerlach C. Element-free Galerkin methods for dynamic fracture in concrete. *Computer Methods in Applied Mechanics and Engineering* 2000; **187**:385–399.
27. Moës N, Belytschko T. Extended finite element method for cohesive crack growth. *Engineering Fracture Mechanics* 2002; **69**:813–833.
28. Ghosh S, Ling Y, Bhaskar M, Ran K. Interfacial debonding analysis in multiple fiber reinforced composites. *Mechanics of Materials* 2000; **32**:561–591.
29. Moorthy S, Ghosh S. A model for analysis for arbitrary composite and porous microstructures with Voronoi cell finite elements. *International Journal for Numerical Methods in Engineering* 1996; **39**:2363–2398.
30. Moorthy S, Ghosh S. Adaptivity and convergence in the Voronoi cell finite element model for analyzing heterogeneous materials. *Computer Methods in Applied Mechanics and Engineering* 2000; **185**:37–74.
31. Ghosh S, Moorthy S. Particle cracking simulation in non-uniform microstructures of metal-matrix composites. *Acta Metallurgica et Materialia* 1998; **46**(3):965–982.

Copyright © 2005 John Wiley & Sons, Ltd.

32. Ghosh S, Mukhopadhyay SN. A two dimensional automatic mesh generator for finite element analysis of randomly dispersed composites. *Computers and Structures* 1991; **41**(2):241–256.
33. Ghosh S, Moorthy S. Three dimensional Voronoi cell finite element model for modelling microstructures with ellipsoidal heterogeneities. *Computational Mechanics* 2004; **34**(6):510–531.
34. Li S, Ghosh S. Debonding in composite microstructures with morphologic variations. *International Journal of Computational Methods* 2004; **1**(1):121–149.
35. Glowinski R, Lawton W, Ravachol M, Tenenbaum E. Wavelet solutions of linear and non-linear elliptic, parabolic and hyperbolic problems in one space dimension. *Computing Methods in Applied Science and Engineering*. SIAM: Philadelphia, PA, 1990.
36. Jaffard S. Wavelet methods for fast resolution of elliptic problem. *SIAM Journal on Numerical Analysis* 1992; **29**(4):965–986.
37. Qian S, Weiss J. Wavelets and the numerical solution of boundary value problems. *Applied Mathematics Letters* 1993; **6**(1):47–52.
38. Barenblatt GI. The mathematical theory of equilibrium cracks in brittle fracture. *Advances in Applied Mechanics* 1962; **7**:55–129.
39. Dugdale DS. Yielding in steel sheets containing slits. *Journal of Mechanics and Physics of Solids* 1960; **8**:100–104.
40. Tan H, Liu C, Huang Y, Geubelle PH. The cohesive law for the particle/matrix interfaces in high explosives. *Journal of the Mechanics and Physics of Solids* 2005; **53**:1892–1917.
41. Babuska I. The finite element method with Lagrange multipliers. *Numerische Mathematik* 1973; **20**:179–192.
42. Brezzi F. On the existence, uniqueness and approximation of saddle-point problems arising from Lagrange Multipliers. *R.A.I.R.O* 1974; **8**(R2):129–151.
43. Xue W-M, Karlovitz LA, Atluri SN. On the existence and stability conditions for mixed-hybrid finite element solutions based on Reissner's variational principle. *International Journal of Solids and Structures* 1985; **21**(1):97–116.
44. Spilker RL, Singh SP. Three-dimensional hybrid-stress isoparametric quadratic displacement elements. *International Journal for Numerical Methods in Engineering* 1982; **18**:445–465.
45. Adalsteinsson D, Sethian JA. A fast level set method for propagating interfaces. *Journal of Computational Physics* 1995; **118**:269–277.
46. Sethian JA. Evolution, implementation, and application of level set and fast marching methods for advancing fronts. *Journal of Computational Physics* 2001; **169**:503–555.
47. Belytschko T, Moes N, Usui A, Parimi C. Arbitrary discontunities in finite element. *International Journal for Numerical Methods in Engineering* 2001; **50**(4):993–1013.
48. Ventura G, Xu JX, Belytschko T. A vector level set method and new discontinuity approximations for crack growth by EFG. *International Journal for Numerical Methods in Engineering* 2002; **54**(6):923–944.
49. Ventura G, Budyn E, Belytschko T. Vector level sets for description of progagating cracks in finite elements. *International Journal for Numerical Methods in Engineering* 2003; **58**(10):1571–1592.
50. Chui CK. *An Introduction to Wavelets.* Academic Press: New York, 1992.
51. Motard RL, Joseph B. *Wavelet Applications in Chemical Engineering*. Kluwer Academic Publishers: Dordrecht, 1994.
52. Haar A. Zur theorie der orthogonalen funkktionen-systeme. *Mathematische Annalen* 1910; **69**:331–371.
53. Meyer Y. Ondelettes et Fonctions Splines. *Seminaire EDP*. Ecole Polytechnique: Paris, 1986.
54. Chui CK, Wang JZ. A general framework of compactly supported splines and wavelets. *Journal of Approximation Theory* 1992; **71**(3):263–304.
55. Daubechies I. Orthonormal bases of compactly supported wavelets. *Communications on Pure and Applied Mathematics* 1988; **41**(7):909–996.
56. Daubechies I. Orthonormal bases of compactly supported wavelets II. *SIAM Journal on Mathematical Analysis* 1993; **24**(2):499–519.
57. Brasseur JG, Wang Q. Structural evolution of intermittency and anisotropy at different scales analyzed using three dimensional wavelet transforms. *Physics of Fluids* 1992; **A4**(11):2538–2554.
58. Everson R, Sirooich L, Sreenicasan KR. Wavelet analysis of the turbulent jet. *Physics Letters A* 1990; **145**:314–322.
59. Lewalle J. Wavelet analysis of experimental data: some methods and the underlying physics. *AIAA 94-2281*, *25th AIM Fluid Dynamics*, Colorado Springs, 1994.
60. Daubechies I. *Ten Lectures in Wavelets*. Society for Industrial and Applied Mathematics: Philadelphia, PA, 1992.

Copyright © 2005 John Wiley & Sons, Ltd.

61. Crisfield MA. A fast incremental/iterative solution procedure that handles 'snap-through'. *Computers and Structures* 1981; **13**:55–62.
62. Crisfield MA. An arc-length method including line searches and accelerations. *International Journal for Numerical Methods in Engineering* 1983; **19**:1269–1289.
63. Schweizerhof KH, Wriggers Y. Consistent linearization for path following methods in non-linear F.E. analysis. *Computer Methods in Applied Mechanics and Engineering* 1986; **59**:261–279.
64. Réthoré J, Gravouil A, Combescure A. An energy-conserving scheme for dynamic crack growth using the eXtended finite element method. *International Journal for Numerical Methods in Engineering* 2005; **63**: 631–659.
65. Yau J, Wang S, Corten H. A mixed-mode crack analysis of isotropic solids using conservation laws of elasticity. *Journal of Applied Mechanics* 1980; **47**:335–341.
66. Tada H. *The Stress Analysis of Cracks Handbook*. Del Research Corporation: Hellertown, PA, 1973.
67. Erdogan F, Sih GC. On the crack extension in plates under plane loading and transverse shear. *Journal of Basic Engineering* 1963; 519–527.
68. Carpinteri A, Colombo G. Numerical analysis of catastrophic softening behavior (snap-back instability). *Computers and Structures* 1989; **31**:607–636.
69. Mariani S, Perego U. Extended finite element method for quasi-brittle fracture. *International Journal for Numerical Methods in Engineering* 2003; **58**:103–126.
70. Sharma K, Singh RK, Kishore NN, Vase KK, Ghosh AK. Application of EFG (element free Galerkin) for crack path prediction. *Proceeding of the International Congress on Computational Mechanics and Simulation 04*, India, 2004; 540–547.

Copyright © 2005 John Wiley & Sons, Ltd.